Remote-sensing estimate of glacier mass balance over the central Nyainqentanglha Range during 1968 – ~2013

Kunpeng Wu [1, 2*], Shiyin Liu [2, 3*], Zongli Jiang [4], Junli Xu [5], Junfeng Wei [4]

[1]School of Resources and Environment, Anqing Normal University, Anqing, 246133, China

[2]Institute of International Rivers and Eco-Security, Yunnan University, Kunming, 650091, China

[3]State Key Laboratory of Cryospheric Sciences, Northwest Institute of Eco-Environment and Resources, Chinese Academy of Sciences, Lanzhou, 730000, China

[4]Department of Geography, Hunan University of Science and Technology, Xiangtan, 411201, China

[5]Department of Surveying and Mapping, Yancheng Teachers University, Yancheng, 224007, China

Correspondence to LIU Shiyin at liusy@lzb.ac.cn or WU Kunpeng at wukunpeng2008@lzb.ac.cn

* These authors contributed equally to this work and should be considered co-first authors

Abstract. With high air temperatures and annual precipitation, maritime glaciers in southeastern Tibet are sensitive to climate change. Current glaciological knowledge of ~~those~~ glaciers in the central Nyainqentanglha Range is still limited because of their inaccessibility and low-quality data. To obtain information on changes in glacier mass balance, a comprehensive study was carried out based on digital-elevation models (DEM) derived from the 1968 topographic maps, the Shuttle Radar Topography Mission (SRTM) DEM (2000), and TerraSAR-X/TanDEM-X (~2013). Glacier area and length changes between 1968 and 2016 were derived from topographic maps and Landsat OLI images. ~~To obtain information on changes in glacier area, length and mass balance, a comprehensive study was carried out based on topographic maps and Landsat TM/ETM+/OLI images (1968 and 2016), and on digital elevation models (DEM) derived from the 1968 maps, from the Shuttle Radar Topography Mission (SRTM) DEM (2000), and from TerraSAR-X/TanDEM-X (~2013).~~ This showed the area contained 715 glaciers, with an area of 1713.42 ± 51.82 km^2, in 2016. Ice cover has been shrinking by 0.68% ± 0.05% a^{-1} since 1968, although in the most recent decade this rate has slowed. The glacier area covered by debris accounted for 11.9% of the total and decreased in SE-NW directions. Using DEM differencing and Differential Synthetic Aperture Radar Interferometry (DInSAR), a significant mass deficit of 0.46 ± 0.10 m w.e. a^{-1} has been recorded since 1968; mass losses accelerating from 0.42 ± 0.20 m w.e. a^{-1} to 0.60 ± 0.20 m w.e. a^{-1} during 1968–2000 and 2000–~2013, with thinning noticeably greater on the debris-covered ice than the clean ice. Surface-elevation changes can be influenced by ice cliffs, as well as debris cover, and land- or lake-terminating glaciers and supraglacial lakes. Changes showed spatial and temporal heterogeneity and a substantial correlation with climate warming.

1 Introduction

The Tibetan Plateau (TP), known as the roof of the world or Third Pole, contains the largest concentration of glaciers and icefield outside the Polar Regions (Yao, 2008). Meltwater from these feeds the headwaters of many prominent Asian rivers (e.g., the Yellow, Yangtze, Mekong, Salween, Brahmaputra, Ganges and Indus) (Immerzeel et al., 2010), and are a key component of the cryospheric system (Li et al., 2008). Glaciers are important climate indicators because their extent and thickness

adjust in response to climate change (Oerlemans, 1994; T. Yao et al., 2012). With a warming climate, many mountain glaciers have shrunk progressively in mass and extent during past decades (IPCC, 2013). However, slight mass gains or balanced mass budgets have been evident for parts of the central Karakoram, eastern Pamir and the western TP in recent years (Bao et al., 2015; Gardelle et al., 2012b; Gardelle et al., 2013; Kääb et al., 2015; Ke et al., 2015; Neckel et al., 2014; T. Yao et al., 2012). The relationships between glacier mass balance and climate change, water supply and the risk of glacier-related disasters, are the subject of much current research.

It is difficult to carry out in-situ observations on the Tibetan Plateau due to its rugged terrain and the great labor and logistical costs. Only 15 glaciers have decades of mass-balance measurements (T. Yao et al., 2012). Fortunately, new methods are now available for estimating large-scale glacier mass balance, such as satellite geodesy. By comparing topographic data from more than two points in time, glacier volume or height changes can be determined and hence ~~thence~~ glacier mass balance, after consideration of ice/firn/snow densities (Bolch et al., 2011; Gardelle et al., 2013; Kääb et al., 2012; Paul et al., 2015; Pieczonka et al., 2013; Shangguan et al., 2014; Brun et al., 2017; Zhou et al. 2018).

Glaciers in south-eastern Tibet are reportedly of the temperate (maritime) type and are influenced by the South Asian monsoon (Li et al., 1986; Shi and Liu, 2000). Based on inventories from maps and remote sensing, or field measurements, a substantial reduction in glacier area and length has been recorded from 1980–2013, as well as a glacier mass deficit from 2005–2009 (Li et al., 2014; Yang et al., 2010; Yang et al., 2008; T. Yao et al., 2012). Most previous studies used satellite laser or optical photogrammetry to calculate the glacier height changes that determined pronounced negative glacier mass balances in the region (Gardelle et al., 2013; Gardner et al., 2013; Kääb et al., 2015; Neckel et al., 2014), although the results did differ slightly from each other. ICESat footprint data showed geodetic glacier-elevation difference trends in south-eastern Tibet during 2003–2008 of 1.34 ± 0.29 m a^{-1} (Kääb et al., 2015), 0.81 ± 0.32 m a^{-1} (Neckel et al., 2014) and 0.30 ± 0.13 m a^{-1} (Gardner et al., 2013), respectively. The large orbital gaps in ICESat footprint data ~~these data~~ mean spatial details cannot be mapped at a fine scale, whereas photogrammetry does provide better spatial detail on glacier-height changes. A comparison between ASTER images and Shuttle Radar Topography Mission (SRTM) data found a mean glacier mass balance of -0.62 ± 0.23 m w.e. a^{-1} in Nyainqentanglha from 2000–2016 (Brun et al., 2017). ~~A comparison between SPOT5/HRS and Shuttle Radar Topography Mission (SRTM) data from January 2011 found a mean glacier thinning of 0.39 ± 0.16 m a^{-1} in south eastern Tibet (Gardelle et al., 2013).~~ However, the lack of local mass-balance measurements means details on the specific response of these glaciers to climate change were lacking, especially for the western region which is the central Nyainqentanglha Range (CNR). ~~Bistatic SAR interferometry is an alternative method to optical photogrammetry and altimetry for analysing topographic change. TanDEM-X was launched in 2010 to join its twin satellite, TerraSAR-X, and operates with it in bistatic mode. This mode overcomes the temporal decorrelation and atmospheric delay disturbance associated with conventional repeat pass interferometry (Jaber et al., 2012).~~ Based on the Shuttle Radar Topography Mission (SRTM) and an interferometrically derived TanDEM-X elevation model, glaciers were determined to have experienced strong surface lowering in the CNR, at an average rate of -0.83 ± 0.57 m a^{-1} from 2000–2014 (Neckel et al., 2017). While this pronounced surface-lowering value came from five debris-covered valley glaciers in the study area, it cannot represent large-scale glaciers' response to climate warming. Furthermore, most meteorological stations, located in inhabited river valleys, are far from the glacierized high mountain regions so their records cannot be used directly as climate background for them. Even ~~when~~ in the same climate environment, glaciers are also responding to local

parameters, such as catchment aspect, topography, and debris cover (Käab, 2005; Neckel et al., 2017; Scherler et al., 2011).

This study aims to map the geodetic glacier mass balances for a large number of glaciers in the central Nyainqentanglha Range. Topographic Maps were drawn from aerial photographs taken in April 1968, and subsequently the Shuttle Radar Topography Mission (SRTM) DEM resulted by X-band SAR Interferometry (InSAR) in February 2000. Single-pass X-band InSAR from TerraSAR-X and TanDEM-X digital elevation measurements provided the basis for another map (Krieger et al., 2007). Bistatic Differential Synthetic Aperture Radar Interferometry (DInSAR) and common DEM differencing were used to estimate the geodetic glacier mass balance in different sub-regions of the CNR between 1968 and ~2013.

2 Study area

The CNR (30°9′~ 30°53′N, 94°0′~ 95°30′E) lies in south-eastern Tibet, north of Linzhi County, east of Jiali County and west of Bomi County, extending about 130 km from west to east. South of this region is the Yigong Tsangpo River, a tributary of the Purlung Tsangpo River and a secondary tributary of the Yarlung Tsangpo River (Fig. 1). The altitudinal differences between mountain peaks and valley bottoms often reach 3000-3500 m. The rugged topography with steep valleys and slopes results from the interplay of a still ongoing tectonic uplift and erosion (Li et al., 1986). High precipitation amounts during the summer monsoon season (May to September) are the main reason for the intense erosion. The CNR is characterized by a strong climatic influence of the Indian summer monsoon entering through the Yarlung Tsangpo valley (Loibl et al., 2014). More than 80% of annual precipitation falls from June to September, while winter months are characterized by cold and dry conditions (Molnar et al., 2010). According to the climatic classification of local meteorological station data, the CNR marks a transition zone between warm-wet subtropical and cold-dry plateau conditions (Leber et al., 1995). Previous studies showed that average annual precipitation in most high-elevation areas in the CNR exceeds 2000 mm. Farther north, the east-west striking ranges act as barriers forcing heavy orographic rainfalls (Böhner, 2006; Maussion et al., 2014). This results in a distinct precipitation gradient from south toward north slope of the CNR (Shi et al., 1988).

~~The southern slopes are exposed to the moist southwest monsoon (Li et al., 1986) which enters the plateau at the Grand Bend of the Yarlung Zangbo. Because the terrain forces the air to rise, the CNR is the most humid region of the Tibetan Plateau and one of the most important and concentrated regions of maritime (temperate) glacier development (Shi et al., 2008; Shi and Liu, 2000). The mean summer air temperature at the equilibrium line altitude (ELA) of glaciers here is usually above 1 °C, and annual precipitation is 2500–3000 mm (Shi et al., 1988).~~

Due to the high elevation, the monsoonal summer precipitation accumulates as snow in the upper reaches of the mountain range, a large number of maritime (temperate) glaciers developed (Shi et al., 2008; Shi and Liu, 2000). The first Chinese Glacier Inventory (CGI) determined that glaciers covered 2537.7 km^2 of our study region, with a total volume of 454.2 km^3 in 1968 (Mi et al., 2002; Pu, 2001); about 8% of the area was covered by debris. Three glaciers in the CNR are larger than 100 km^2, the Xiaqu (CGI code: 5O281B0702), Kyagqen (CGI code: 5O281B0729) and Nalong (CGI code: 5O281B0768). The Kyagqen, on the south slope of the CNR, 35.3 km long and 206.7 km^2, with a terminus at 2900 m a.s.l., is the largest of these (Li et al., 1986). Above 4000 m a.s.l. it has a broad basin in which several ice streams converge to form a large accumulation zone (165 km^2) that accounts for over 80% of the glacier's total area. Below this, the glacier enters a narrow ice-filled valley where its velocity increases; the resultant great driving force pushing the glacier terminus to a subtropical

elevation at 2900 m a.s.l. The narrow glacier tongue, 1000 m wide and 17 km long, passes through the subalpine shrub-meadow zone, the mountain dark coniferous forest zone and the mixed broadleaf-conifer forest zone (Li et al., 1986).

3 Data

3.1 Topographic Maps

Our study uses eight topographic maps at a scale of 1:100 000 (Fig. 1 and Table 1). They were compiled by the Chinese Military Geodetic Service from air photos acquired in April 1968. Their geographic projection was based on the Beijing Geodetic Coordinate System 1954 (BJ54) geoid and the Yellow Sea 1956 datum. Using a seven parameter transformation method, these maps were re-projected into the World Geodetic System 1984 (WGS1984)/Earth Gravity Model 1996 (EGM96) (Xu et al., 2013). The contour lines were digitized from topographic maps manually, and then using the Thiessen polygon method, converted into a raster DEM with a 30 m grid cell (hereafter called TOPO DEM) (Shangguan et al., 2010; Wei et al., 2015; Zhang et al., 2016a). According to the national photogrammetric standard of China, the vertical accuracy of the TOPO DEM is better than 16 m on glaciers with gentle slopes (~24 °) which is common for most of the glacierized areas in the CNR.

3.2 Shuttle Radar Topography Mission

Acquired by radar interferometry with C-band and X-band in early February 2000, the SRTM DEM can be referred to the glacier surface in 1999 with slight seasonal variances (Gardelle et al., 2013; Pieczonka et al., 2013; Zwally et al., 2011). Due to large data gaps in the X-band DEM (Rabus et al., 2003), only 20% of the CNR glaciers are covered. Hence, the SRTM C-band DEM was used in this study for glacier surface elevation change. The unfilled finished SRTM C-band DEM is freely available on *http://earthexplorer.usgs.gov/*. The spatial resolution of SRTM C-band DEM is 1 arc-second (approximately 30 m) and geographic projection is WGS84/EGM96. While the penetration depth of the SRTM C-band radar beam into snow and ice is a critical issue when the SRTM DEM is used for geodetic mass-balance calculations. Previous studies indicated that the penetration depth affected by the carrier frequency, the density of snow and ice, and its water content (Berthier et al., 2006; Kääb et al., 2015). Due to the high water content of maritime (temperate) glaciers, it is presumed that the X-band does not penetrate into snow and ice. The elevation difference between the SRTM C-band and X-band DEM can be considered as a first approximation for the penetration depth of the SRTM C-band (Berthier et al., 2018; Gardelle et al., 2012a; Kääb et al., 2012).

3.3 TerraSAR-X/TanDEM-X

TerraSAR-X was launched in June 2007, and then its twin satellite, TanDEM-X was launched in June 2010 by the German Aerospace Center (DLR). Fly in close orbit formation, the two satellites acting as a flexible single-pass SAR interferometer (Krieger et al., 2007). Four pairs of X-band bistatic TerraSAR-X/TanDEM-X data points in the experimental Co-registered Single look Slant range Complex (CoSSC) format, acquired in bistatic InSAR stripmap mode, were used in this study (Fig. 1, Tables 1, 2). The frame sizes of these images were approximately 40 × 60 km, with resolutions of approximately 2.5 m in both the ground range and azimuth direction. To avoid seasonal variations induced by melting and snow cover, images were chosen mainly from those taken in February or adjacent months. ~~Images were processed separately in interferometric steps and then mosaicked~~

~~(Werner et al., 2000).~~

3.4 Landsat images

~~The relationship between glacier mass balance and changes in glacier extent is worth studying.~~ The present glacier outlines were generated from Landsat images. In order to acquire the relationship between glacier area and mass balance, ~~It~~ it is best that Landsat images be acquired in the same year as the SRTM and TerraSAR-X/TanDEM-X data. Unfortunately, due to the influence of the Indian monsoon, the CNR was almost permanently covered by snow and cloud, so higher quality images could not be acquired in 2000–2010. The Operational Land Imager (OLI) sensor, on board Landsat-8, provides an excellent new mid-resolution image source for compiling regional-scale glacier inventories and can provide good-quality multispectral images. Acquired from the United States Geological Survey (USGS), the Landsat OLI images are orthorectified with the SRTM~~, and almost no horizontal shift was observed~~. We selected a Landsat OLI scene from 2016 as reference. For the OLI scenes no horizontal shift was observed, whereas the topographic maps had small systematic shifts of 6 to 12 m.

4 Methods

4.1 Glacier Delineation

Based on scanned and well-georeferenced topographical maps, the outlines of glaciers in the CNR in 1968 were digitized manually. ~~And then the outlines were validated by reference to the original aerial photographs.~~

Glacier outlines in 2016 were delineated using a ratio threshold method, a division of the visible or near-infrared band and shortwave infrared band of Landsat OLI images (Paul et al., 2009; Racoviteanu et al., 2009). A 3 × 3 median filter was applied to eliminate isolated ice patches < 0.01 km^2 (Bolch et al., 2010b; Wu et al., 2016). In order to discriminate proglacial lakes, seasonal snow, supraglacial boulders and debris-covered ice, scenes without snow, or cloud-free image scenes acquired at nearly the same time, were used for reference when making manual adjustments. Generated from the SRTM-C DEM automatically, topographical ridgelines (TRLs) were used to divide~~d~~ the final contiguous ice coverage into individual glacier polygons (Guo et al., 2015).

Uncertainty in the glacier outlines arises from positional and processing errors associated with glacier delineation (Bolch et al., 2010a; Racoviteanu et al., 2008). No distinct horizontal shift was observed in Landsat images and the impact of seasonal snow, cloud and debris cover was eliminated manually (Bolch et al., 2010a; Guo et al., 2015). The best way to assess processing errors is to compare our results with independently digitized glacier outlines from high-resolution air photos (Bolch et al., 2010a; Paul et al., 2003). Compared glacier outlines derived from Landsat-images ~~Landsat image outlines~~ with real-time kinematic differential GPS (RTK-DGPS) measurements~~ and Google EarthTM images~~, average offsets of ±10 m and ±30 m were acquired for the delineation of clean and debris-covered ice (Guo et al., 2015), whereas average offsets between topographic-maps outlines and Corona images was ±6.8 m (Wu et al., 2016). On the basis of these average offsets, ~~Hence,~~ mean relative errors of ±0.8% and ±3.0% were determined for glacier areas in 1968 and 2016, respectively.

4.2 Glacier Length

The length of the glacier centreline, a key parameter in glacier inventory, is a most important one for modelling future glacier evolution (Le Bris and Paul, 2013). It has been digitized manually in traditional studies, but this method is inefficient and cannot be replicated. With the rapid development of Geographic Information System (GIS) technology, a few automated techniques have been proposed

(Kienholz et al., 2014; Koblet et al., 2010; Le Bris and Paul, 2013; Schiefer et al., 2008). Using a hydrological approach, Schiefer et al. (2008) derived a line representing the maximum flow path water would take over the glacier surface, but these lengths are 10–15% longer than distances measured along actual centrelines. Le Bris and Paul (2013) presented an alternative method, based on a so-called "glacier axis" concept, following a centreline from the highest to the lowest glacier elevation. A limitation of this approach is that the derived line does not necessarily represent the longest glacier centreline or that of the main branch. Kienholz et al. (2014) suggested another method based on a "cost grid—least-cost route approach"; however, it is quite complicated to calculate and some lines have to be adjusted manually.

~~A new strategy is implemented here (X. Yao et al., 2015) b~~Based on a glacier-axis concept derived from glacier morphology that only requires glacier outlines and a digital elevation model (DEM) as input, glacier centerline was derived semi-automatically in this study (X. Yao et al., 2015). From GIS modelling techniques, an automatic method is applied to derive the heads, termini and centrelines of glaciers. First, the heads and termini are identified for every glacier. Second, the glacier outline is divided into two curved lines based on its head and terminus. Third, using the method of Euclidean distance, the glacier polygon is divided into two regions. The common boundary of these two regions can be referred to the glacier centreline. This method was applied in the Kangri Karpo Mountains and error estimation was performed by comparing the results with high-resolution aerial imagery at the terminus (Paul et al., 2015). The uncertainties were no more than 6 and 7.5 m in 1968 and 2016, respectively (Wu et al., 2018).

4.3 Glacier elevation changes

The methodology of glacier elevation changes in this study is similar to the previous work of Wu et al. (2018). Bistatic interferograms contain both flat earth and topographic phases from which glacier-elevation changes can be derived (Li and Lin, 2017; Li et al., 2018; Neckel et al., 2013; Paul et al., 2015). Two methods can be used. The first, based on differential SAR interferometry (DInSAR), uses orbital information from bistatic SAR images and reference DEMs (here SRTM DEM and TOPO DEM) to simulate the flat earth and topographic phases, and then removes them from the original bistatic interferogram to leave a differential interferogram. The second, common DEM differencing, generates a new DEM from bistatic SAR images, based on InSAR technology, and then performs common DEM differencing with respect to reference DEMs (Neckel et al., 2013). In the DInSAR method, most parts of the topographic phase have been simulated and removed and the reliability of phase unwrapping increased by the smaller phase gradients (Neckel et al., 2013) so the topographic residual phase can be transformed directly to an elevation change. The DInSAR and common DEM differencing methods were used to detect glacier-elevation changes in the CNR between 1968 and ~2013.

To improve the phase-unwrapping procedure and minimize errors, the unfilled finished SRTM C-band DEM was employed. The use of the DInSAR method to acquire elevation changes from bistatic SAR images can be described by

$$\Delta\varphi_{elevation} = -\frac{2\pi B_{\perp}\Delta h}{\lambda R \sin\theta} = -\left(\frac{2\pi B_{\perp}\Delta h_{srtm}}{\lambda R \sin\theta} + \frac{2\pi B_{\perp}\Delta h_{residual}}{\lambda R \sin\theta}\right) \quad (1)$$

where $B_{\perp}$ is the perpendicular baseline, λ is the wavelength of the radar signal, R is geometric distance from the satellite to the scatterer, θ is the incidence angle, and Δh is elevation, which can be split into elevation in SRTM C-band DEM (Δh_{srtm}) and the elevation changes ($\Delta h_{residual}$) due to glacier

thinning or thickening (Kubanek et al., 2015; Li et al., 2018).

It is assumed that no height change occurs in the off-glacier regions. Precise horizontal offset registration between the SRTM C-band DEM and the TerraSAR-X/TanDEM-X acquisitions is mandatory. An initial lookup table was calculated, based on the relationship between the map coordinates of the SRTM C-band DEM segment covering the TerraSAR-X/TanDEM-X master file and the SAR geometry of the respective master file. Due to the side-looking geometry of TerraSAR-X/TanDEM-X, distortion in the foreshortening, layover and shadow regions, can result in some errors. These distortions induce gaps in the lookup table which were filled by linear interpolation. The horizontal offsets between both datasets were calculated by GAMMA's offset_pwrm module for cross-correlation optimization of the simulated SAR images. The horizontal registration and geocoding lookup table was refined with these offsets and used to translate the SRTM C-band DEM from geographic into SAR coordinates. A differential interferogram was then generated from the TerraSAR-X/TanDEM-X interferogram and the simulated phase of the co-registered SRTM C-band DEM. This was filtered by an adaptive filtering approach and the flattened differential interferogram unwrapped with GAMMA's minimum cost flow (MCF) algorithm. The unwrapped differential phase could be transformed to absolute elevation changes from the computed phase-to-height sensitivity and select ground control points (GCPs) of the off-glacier regions of the SRTM C-band DEM. However, the baseline refinement cannot completely eliminate error, so a residual exists in the differential interferogram. This residual can be regarded as a linear trend estimated by a two-dimensional first-order polynomial fit in off-glacier regions. Using polynomial fitting, the residual was removed from maps of absolute differential heights. Finally, the resulting datasets were translated from SAR coordinates into a metric cartographic coordinate system using the refined geocoding lookup table (Paul et al., 2015).

Common DEM differencing with the TOPO DEM and SRTM C-band DEM was employed to acquire the glacier-elevation change from 1968 to 2000 (Liu et al., 2017; Nuth and Kääb, 2011; Pieczonka et al., 2013; Wei et al., 2015). Based on the relationship between elevation difference, slope and aspect, relative horizontal and vertical distortions between the two datasets were corrected statistically (Nuth and Kääb, 2011). At first, a difference map was constructed with the TOPO DEM and SRTM C-band DEM. Before adjustments, histogram statistics for off-glacier regions showed elevation differences concentrated at 6.73 m. Outliers are usually found around data gaps and near DEM edges and can be excluded using 5% and 95% quantile thresholds based on statistical analysis (Pieczonka et al., 2013). Then, based on the substantial cosinusoidal relationship between standardized vertical bias and topographical parameters (slope and aspect), the vertical biases and horizontal displacements could be rectified simultaneously (Fig. 2). The biases, caused by different spatial resolutions between the two datasets, could be refined using the same relationship between elevation differences and maximum curvatures for both on- and off-glacier regions (Gardelle et al., 2012a). After these adjustments, the elevation differences in off-glacier regions were concentrated at -0.24 m. It was concluded that elevation differences in the off-glacier regions had stabilized after these refinements making the processed DEMs suitable for estimating changes in the glaciers' mass balance.

4.4 Penetration depth

When the SRTM DEM is used for geodetic mass-balance calculations, the penetration depth of the radar signal into snow and ice has to be considered (Berthier et al., 2006; Gardelle et al., 2012a; Neelmeijer et al., 2017; Rignot et al., 2001; Vijay et al, 2016). Previous studies indicated that the

penetration depth affected by the carrier frequency, the density of snow and ice, and its water content (Berthier et al., 2006; Kääb et al., 2015). Given that the TerraSAR-X/TanDEM-X were observed mostly in February, when the SRTM was performed, and the carrier frequencies of the TerraSAR-X/TanDEM-X and the SRTM X-band satellites are almost the same, it is assumed that no penetration warranting consideration exists between these two datasets (Li and Lin, 2017). The elevation difference between SRTM C-band and X-band DEMs can be considered to be the SRTM C-band radar beam penetration into snow and ice (Gardelle et al., 2012a). The penetration depth in the off-glacier regions was assumed to be zero as the acquisition dates of SRTM and our TerraSAR-X/TanDEM-X images avoided the main rainy season (Yang et al., 2013), so elevation differences between SRTM C-band and X-band DEMs could be evaluated with common DEM differencing.

The penetration depth differences were analysed and corrected in each 100 m elevation bin. Because the penetration difference should not exceed 10 m (Gardelle et al., 2012a), all of the difference values greater than ±10 m were defined as outliers and did not consider for the penetration estimation. The median values of each elevation bin were used to correct the SRTM C-band DEM but only for areas with elevations below 6200 m a.s.l. In the CNR, the penetration depth difference for clean ice/firn/snow was about 0.88 m below 5200 m, and 1.28 m between 5200 and 6200 m. There have no enough pixels per elevation bin were available to generate reliable results at higher elevations. Glacier area above 6200 m occupies about 0.78% of the total glacier area in this study. According to the linear trend calculated for the several highest bins in Fig. 3, a value of 2.26 was assumed for the area above 6200 m. Interestingly, some of the lower elevation bins in debris-covered area show negative correction values. Because the stable areas were also partly covered with snow, the radar penetration difference due to this snow cover was removed during the vertical matching of SRTM C-band and X-band DEMs., Low-elevation bins in debris-covered area have less snow cover than the stable areas, and this will result in negative radar penetration differences. Hence, penetration corrections were not applied for the debris-covered regions. In total, the average penetration depth of the SRTM C-band radar is 1.16 m for clean ice/firn/snow in the CNR. This value is consistent with previous studies finding an average penetration depth of 1.1 m in Yigong Tsangpo (Zhou et al., 2018).

~~The result showed that the average penetration depth of the SRTM C-band radar is 1.16 m in the CNR. This value is consistent with previous studies finding an average penetration depth of 1.1 m in Yigong Tsangpo (Zhou et al., 2018).~~

4.5 Mass balance and accuracy estimation

In order to convert glacier-elevation changes to a geodetic mass balance, the glacier area and ice/firn/snow density must be considered. The geometric union of the 1968 and ~2013 glacier masks was used to identify area changes (Li et al., 2012; Neckel et al., 2013). An ice/firn/snow density of 850 kg m^{-3}, with an uncertainty of 60 kg m^{-3}, was applied to assess the water equivalent (w.e.) of mass changes from elevation differences (Huss, 2013; Li et al., 2018; Wei et al., 2015). ~~As the equilibrium line altitude (ELA) increases gradually from south to north in the CNR (T. Yao et al., 2012), it is difficult to separate the ablation and accumulation zones so the density value was applied to both. The final error in geodetic glacier mass balances results from errors in surface elevation measurements (Gardelle et al., 2013).~~

Field measurement of off-glacier elevations is the best way to assess the accuracy of the DEMs employed in this study. While it is difficult to carry out large-scale GPS real-time kinematic (GPS-RTK)

field measurements in off-glacier region, elevations from the ICESat Geoscience Laser Altimeter System (GLAS) could be employed for a first accuracy assessment. These data are freely available from the National Snow and Ice Data Center (NSIDC) (release 634; product GLA14). Surface elevations of the DEMs were extracted at each ICESat footprint location. To ensure the accuracy of comparison, ICESat points were removed from the analysis if the elevation difference between GLA14 and multi-source DEMs exceeded 100 m in off-glacier region. A mean and standard deviation of 2.14 ± 1.46 m and 1.95 ± 1.76 m were found for the TOPO and SRTM C-band DEMs, respectively. For the InSAR-derived TerraSAR-X/TanDEM-X DEM, the GCPs that converted the unwrapped interferogram into absolute heights were selected from the off-glacier regions of the SRTM C-band DEM; the accuracy of TerraSAR-X/TanDEM-X DEM are similar to those of the SRTM C-band DEM.

In the process of deriving glacier elevation changes, it is assumed that no height change occurred in the off-glacier regions from 1968 to ~2013. For an error estimate of the derived surface elevation changes, the residual elevation differences in off-glacier regions needs to be estimated. The ~~mean~~ average elevation differences (~~MED~~AED) between the final difference maps in off-glacier regions ranged from -1.23 to 1.12 m (Table 3, supplementary figure S1). The standard deviation (SD) in off-glacier regions will probably overestimate the uncertainty of the larger sample because averaging in larger regions reduces the error. The uncertainty can be estimated by the standard error of the mean (SE) (Berthier et al., 2010):

$$SE = SD/\sqrt{N} \quad (2)$$

where N is the number of the included pixels. To minimize the effect of autocorrelation, a decorrelation length based on the spatial resolution is recommended. From previous studies, decorrelations of 600 m and 200 m were employed for different DEMs with the spatial resolution of 30 m and 10 m (Bolch et al., 2011; Paul et al., 2015). The overall errors of derived surface-elevation changes can then be estimated using SE and ~~MED~~ AED in off-glacier regions:

$$\sigma = \sqrt{AED^2 + SE^2} \quad (3)$$

Finally, the overall mass balance errors were determined using the estimated errors of glacier area and surface elevation change, and the ice density uncertainty of 60 kg m^{-3} (Neckel et al., 2013).

5 Results

5.1 Area change

There were 715 glaciers with a total area of 1713.42 ± 51.82 km^2 in 2016 in the CNR~~, with a mean glacier size about 2.40 ± 0.07 km^2~~ (Fig. ~~2~~4). While large glaciers dominate the area (those >1 km^2 occupy 93.5% of the total area) small glaciers dominate the number (those ≤0.5 km^2 occupy 69.4% of the total number) (Fig. ~~2a~~4a). Area distribution by elevation bands is normal. About 82.2% lies in the 4500–5800 m elevation range, 4.9% is below 4200 m, and only 2.4% above 6200 m. The median elevation is around 5248 m (Fig. ~~2b~~4b). Kyagqen Glacier, the largest glacier (153.07 ± 0.43 km^2) has the lowest tongue at 2882 m a.s.l. The mean glacier surface slope in the CNR is 22.8 º, with most in the 12 º-32 ºrange, accounting for 93.5% of total area. Glaciers having a SE, S or E aspect account for 85.5% of their area (Fig. ~~2c~~4c).

The central Nyainqentanglha Range contains almost 100 glaciers with significant debris cover, about 203.23 km^2 or ~11.9% of the whole ice cover (Fig. ~~3~~5). Among all the debris-covered glaciers, there were 12 glaciers with areas of debris cover that exceeded 5 km^2. Nalong Glacier has the most in the CNR, 21.88 km^2 or ~28.0% of its area. On Kyagqen Glacier, the debris cover only accounts for 3.2%

of its area. Some 89.4% of the debris-covered area is in the 3700-5100 m elevation range, 7.4% is below 3700 m, and only 3.2% above 5100 m. The lowest elevation of debris cover (2882 m) coincides with the lowest limit of Kyagqen Glacier. The upper limit of debris cover (5754 m) is on Glacier 5N225E0033, on the north slope of the CNR.

Comparing the total area of all glaciers in 1968 with that in 2016, ice cover in the CNR has diminished by 824.32 ± 55.65 km^2 (32.5% ± 2.2%) or 0.68% ± 0.05% a^{-1} (Table 4). Small glaciers shrank the most, but large glaciers dominated the absolute area loss (Fig. ~~2d~~4d). Analysis of glacier hypsography showed that the ice cover below 2800 m, with an area of 0.32 km^2, had disappeared completely, absolute area loss increased gradually with altitude through the 2800–5200 m a.s.l. range, then decreased gradually from 5200–6200 m a.s.l., remaining almost unchanged above 6200 m. The average minimum elevation of the glaciers increased by 258 m, while their median elevation rose about 97 m from 5151 to 5248 m. Disintegration of more glaciers compensated for the disappearance of a few glaciers so the overall number of glaciers increased. Those that had disappeared were small and situated at relatively low altitudes.

5.2 Length change

When comparing the termini of all glaciers in the CNR from 1968–2016 most had retreated. Based on different glacier size, slope and aspect, 33 glaciers were selected from all the retreating glaciers for analysis of length changes (Fig. ~~4~~6, ~~Table 5~~supplementary figure S2 and table S1). All selected glaciers ~~These~~ experienced a mean recession of 1432 m (29.8 m a^{-1}), ranging from 217 m to 8826 m. Glacier 5O281B0567~~, with a mean recession of 4.5 m a^{-1}~~, experienced the least recession (4.5 m a^{-1}), its ~~centreline~~ length decreasing from 4742 m to 4525 m. Glacier 5O281B0575 ~~at 183.9 m a^{-1}~~ experienced the most recession (105.1 m a^{-1}), its length decreasing from 24703 m to 19657 m. The terminus elevations of these selected glaciers rose an average of 113 m, varying from 23 m (3759 to 3782 m a.s.l.) to 323 m (3981 to 4304 m a.s.l.).

5.3 Mass balance

Significant glacier surface lowering has been observed in the CNR since 1968 with mass losses tending to increase during the most recent decade. Glaciers, with an area of 2624.30 km^2, experienced a mean thinning of 24.48 ± 0.70 m (0.54 ± 0.10 m a^{-1}), or a mean mass deficit of 0.46 ± 0.10 m w.e. a^{-1}, equivalent to an overall mass loss of 64.21 ± 1.10 Gt from 1968 to ~2013. The rate of thinning increased during the investigated periods. Glaciers thinned by 15.69 ± 1.25 m, representing a mean mass loss of 0.42 ± 0.20 m w.e. a^{-1} from 1968 to 2000. Surface lowering was 9.24 ± 0.79 m with a mean mass loss of 0.60 ± 0.20 m w.e. a^{-1} from 2000 to ~2013 (Fig. ~~5~~ 7 and Table ~~6~~5). More details of elevation change were showed in Supplementary Figures S3-S6.

Heterogeneous mass balances were detected in the CNR from 1968 to ~2013. Glaciers in south slope, with an area of 1896.36 ± 20.39 km^2, experienced a mean mass deficit of 0.46 ± 0.09 m w.e. a^{-1} from 1968 to ~2013, with means of 0.42 ± 0.19 m w.e. a^{-1} and 0.56 ± 0.17 m w.e. a^{-1} for 1968–2000 and 2000–~2013, respectively. Losses of 0.48 ± 0.08 m w.e. a^{-1} in north slope were ~~larger slightly than~~close to those in south slope from 1968 to ~2013. Glaciers with an area of 727.94 ± 4.31 km^2 in the former experienced a mean mass loss of 0.40 ± 0.20 m w.e. a^{-1} from 1968 to 2000, and then increased significantly to 0.72 ± 0.31 m w.e. a^{-1} from 2000 to ~2013.

Changes varied significantly between the different time intervals and individual glaciers, even for

those in the same basin with a similar climate. In 5O28 basin, Star Glacier (5O282A0103) experienced the largest mass loss from 1968 to ~2013 (0.62 ± 0.11 m w.e. a^{-1}) with losses much higher in the later period from 2000 to ~2013 (1.09 ± 0.29 m w.e. a^{-1}). Meanwhile Cape Glacier (5O282A0071), in the same drainage basin, experienced the smallest losses (0.24 ± 0.11 m w.e. a^{-1}) from 1968 to ~2013, with even less from 1968 to 2000 (0.07 ± 0.21 m w.e. a^{-1}). Accelerating mass losses occurred on most sample glaciers, except for one glacier in the 5N225E basin and two in 5O281B, where the loss rate slowed.

6 Discussion

6.1 Uncertainty

Uncertainty in the delineation of glacier outlines comes from both positional and processing components (Bolch et al., 2010a). In this study, the accuracy of the outlines was assessed by comparing our results with independently digitized glacier outlines from high-resolution aerial photography, such as real-time kinematic differential GPS (RTK-DGPS) measurements, Google EarthTM images with a spatial resolution better than 1 m, and Corona images. An uncertainty model suggested by Pfeffer et al. (2014) ($e(s) = k \times e \times S^p$ ($k = 3$, $e = 0.039$, $p = 0.7$)) was employed to assess our uncertainty estimate. The results determined a value of 21.47 km^2 for glacier delineation uncertainty in the CNR in 2016. This value is smaller than our estimate of about 51.82 km^2. The main reason for this difference is probably an underestimation by the uncertainty model for the CNR, where more debris-covered ice and exposed bedrock, surrounded by an ice cover, exist. Thus, our uncertainty estimate for the delineation of glaciers study should be reliable.

The error in the derived glacier mass balance can result from both systematic and random components (Li et al., 2018). The latter comes from the precision of TerraSAR-X/TanDEM-X acquisitions and SRTM DEMs, as well as the total glacier area measured. The systematic component includes errors in the seasonal effects and penetration depth.

Since geodetic measurements should determine mass balances corresponding to an integer number of balance years, the seasonal variance of glacier mass balances needs to be considered (Gardelle et al., 2012b). In the CNR, maritime (temperate) glaciers develop and receive abundant summer monsoon precipitation. Most accumulation and melting occur simultaneously in the summer. TerraSAR-X/TanDEM-X and SRTM DEMs are usually acquired in February. To evaluate seasonal effects, glacier mass budgets determined from TOPO DEMs should be adjusted to the state of glaciers in February based on mass balance variations. The annual distribution of mass balance is difficult to establish in the study area because field measurements are lacking. It has been assumed, conservatively, that precipitation is totally converted into mass accumulation. Based on the Dataset of Daily $0.5° \times 0.5°$ Grid-based Precipitation in China (V2.0), that for February to April in 1968 was 321 mm, which could create errors of up to ~0.01 m w.e. a^{-1} for the mass balances of 1968–2000 and 1968–~2013. Compared to other factors in this study, any errors arising from the seasonal variance of mass balances can be considered negligible.

Another critical unknown is C-band radar penetration into snow and ice when SRTM C-band DEMs are used for geodetic mass-balance calculations. Penetration depths of 2.1–4.7 m at 10 GHz were measured in the Antarctic (Davis and Poznyak, 1993), where the depth decreases as the temperature and water content of the surface snow increases (Surdyk, 2002). Glaciers in the CNR are predominantly influenced by the monsoon and have higher snow moisture and temperatures than the Antarctic (Shi and Liu, 2000). Hence, the assumption is that the penetration of the X-band radar is

small, 1.16 m as estimated by comparing SRTM C- and X-band DEMs in this study. This value is slightly smaller than that of Gardelle et al. (2013), however, its possible penetration can be considered. The correction for C-band radar penetration led to average mass changes of +0.03 m w.e. a^{-1} for 1968–2000 and -0.08 m w.e. a^{-1} for 2000–~2013.

6.2 Glacier inventory and shrinkage

The median elevation of a glacier is widely used to estimate the long-term Equilibrium Line Altitude (ELA) (Braithwaite and Raper, 2010), and is suitable for analysing the governing climatic conditions (Ke et al., 2016). Heterogeneous median elevations were detected in the CNR, and the spatial distribution of them reflects their climate dependence. This study area is located north of the Yarlung Tsangpo River where an important moisture transport path of the Indian monsoon enters the plateau. From the Great Bend of the Yarlung Zangbo, the median elevation increases in SE-NW directions (Fig. ~~3~~5). On the SE slope of the CNR, the Indian monsoon brings abundant moisture, resulting in a relatively maritime climate and a lower median glacier elevation (below 5000 m). Because the high mountain ranges block water vapour transport to the leeward side, a higher median glacier elevation (above 5300 m) is found on the NW slope. Conversely, the amount of debris cover for the median elevation classes decreases from 25.2% on the SE slope (median elevation <4500 m) to only 2.9% on the NW slope (median elevation >5500 m). The main reasons for this are probably an intensive debris supply from the steep rock walls facing south, the different geology of the SE and NW slopes, and autocorrelation effects between glaciers and the debris cover (Frey et al., 2012; Käab, 2005; Ke et al., 2016).

Due to the influence of the Indian monsoon, the CNR was almost permanently covered by snow and cloud, so the higher-quality optical-satellite images were rarely available from 2000–2010. To preserve the temporal consistency of the second Chinese glacier inventory (CGI-2, based on Landsat images acquired mainly from 2006–2010), a glacier inventory of the CNR was deliberately omitted. Apart from the CGI-2 there have been some other glacier inventories in the CNR. Using 356 Landsat ETM+ scenes in 226 path-row sets from 1999–2003, Nuimura et al. (2015) compiled the GAMDAM inventory (Glacier Area Mapping for Discharge from the Asian Mountains). There was a larger discrepancy between this and the 2000 Chinese glacier inventory in the western Nyainqentanglha Range, probably because the GAMDAM inventory excluded thin ice on headwalls, the effects of shadow and seasonal snow cover, and tended to include smaller areas than those recommended by the GLIMS guidelines (Arendt et al., 2015; Wu et al., 2016). An improved glacier inventory of the SE Tibetan Plateau (SETPGI) was compiled from Landsat images acquired from 2011–2013, coherence images from ALOS/PALSAR images and the SRTM DEM (Ke et al., 2016). Comparing the SETPGI with our 2016 inventory, a slight discrepancy of 3.7% was found which can be accounted for by a change in glacier area of -0.62% a^{-1} from ~2010 to 2016. Ji et al. (2014, 2015) assessed areal changes for seven glaciers in the CNR (Star, Maguo Lung, Ruoguo, Jiangpu, Nalong, Cape, North Cape and Yangbiegong) from aerial photos and Landsat images acquired between 1968 and 2011. Studies showed the ice cover in the CNR had diminished by about 38.2% (1.23% a^{-1}) and 9.8% (0.82% a^{-1}) from 1970–1999 and 1999–2011 ~~(Table 7)~~. It was concluded that the glaciers in the study area have shrunk continuously since 1968 (1.23% a^{-1} from 1970–1999, 0.82% a^{-1} from 1999–2011 and 0.62% a^{-1} from ~2010 to 2016),~~The glaciers in the study area have shrunk continuously since 1968,~~ although the rate has eased during the most recent decade.

~~The ice cover in the CNR was reduced by about 0.68% ± 0.05% a^{-1} between 1968 and 2016.~~

~~Compared with the recession of mountain glaciers in western China, those in the study area have experienced very strong retreat rates. Except for the Altay (0.75% a^{-1}) and Kangri Karpo Mountains (0.71% a^{-1}) (Paul et al., 2015; X. Yao et al., 2012), glacier shrinkage in the CNR has been larger than in any other region of western China (Table 7).~~

6.3 Changes of glacier elevation and mass balance

Previous studies agreed that glaciers in the CNR were losing mass, although the results did differ from each other. Based on SRTM and SPOT5 DEMs (24 November 2011), a mean thinning of 0.39 ± 0.16 m a^{-1} was found by Gardelle et al. (2013), whereas different rates of 1.34 ±0.29 m a^{-1}, 0.81 ±0.32 m a^{-1} and 0.30 ±0.13 m a^{-1} from 2003–2009 were recorded by Kääb et al. (2015), Neckel et al. (2014) and Gardner et al. (2013), respectively, using ICESat and SRTM. In this study, SRTM DEM and TerraSAR-X/TanDEM-X acquisitions yielded a mean ~~mass~~ thinning of 0.54 ±0.05 m a^{-1} from 2000 to ~2013. Different estimates of SRTM C-band penetration have resulted in thinnings at variance with those determined by Kääb et al. (2015). An average SRTM C-band penetration of 8–10 m (7–9 m when based on winter trends assumed to reflect February conditions) was used for the eastern Nyainqentanglha Mountains in the Kääb et al. (2015) study, much greater than the 1.16 m assumed in this study. Previous studies suggested an average penetration of 2.4 m in Bhutan and 1.4 m around the Everest (Gardelle et al., 2013), 2.26 m for clean ice below 6000 m in the Mt. Everest region (Li et al., 2018), 2.5 ±0.5 m for a wider area including east Nepal and Bhutan (Kääb et al., 2012), 1.67 ± 0.53 m in the western Nyainqentanglha Mountains (Li and Lin, 2017), and 1.24 m in the Kangri Karpo Mountains (Wu et al., 2018). Because the CNR lies in the centre of the eastern Himalaya, the western Nyainqentanglha Mountains and the Kangri Karpo Mountains, the glacier characteristics are similar (Shi and Liu, 2000). Since penetration depth varies with temperature and water content (Surdyk, 2002), an average penetration of 1.16 m, in agreement with previous studies, was deemed acceptable and suitable for estimating glacier elevation changes in the CNR.

Brun et al. (2017) recorded a mean mass deficit of 0.62 ±0.23 m w.e. a^{-1} between 2000 and 2016 in the Nyainqentanglha Range, based on ASTER optical satellite stereo pairs. Because this result relies exclusively on satellite optical data, it is not affected by signal penetration. Our determination of a mean mass loss of 0.60 ±0.20 m w.e. a^{-1} from 2000 to ~2013 in the CNR agrees with that Brun et al. (2017) and suggests our results are reliable. A larger discrepancy is noted with the Zhou et al. (2018) results in Yigong Tsangpo from declassified KH-9 images (21 December 1975) and SRTM DEMs; 0.11 ±0.14 m w.e. a^{-1} vs. our result of 0.42 ±0.20 m w.e. a^{-1} from 1968 to 2000. There are likely ~~two~~ three reasons for this discrepancy: first, a difference in dates of the declassified KH-9 images and topographic maps; second, a difference in the glacier area measured. The Yigong Tsangpo study measured a glacier area of 1055 km^2 while ours was 2622.95 km^2. Third, a difference in filling no-data voids in the accumulation areas. Large differences in acquisition dates, glacier areas and no-data voids in the accumulation areas ~~and glacier areas~~ may result in significant disparities in the glacier mass balances determined.

Ice in the comparatively flat lower parts of the larger valley glaciers is much thicker than that in the steep higher glacier reaches, due to the generalized flow law of ice (assumption of perfect plasticity) (Cuffey and Paterson, 2010). This suggests that large areas of ice may become subject to melting in the event of climate warming. Whereas the mass-loss patterns on a debris-covered tongue are complicated, with supraglacial lakes, ice cliffs and a heterogeneous debris cover (Pellicciotti et al., 2015). Although melting is considered to be less on glacier parts covered in debris, due to its insulating effect (Benn and Lehmkuhl, 2000), the surface properties may only have a limited influence on the melt: Thinning was

noticeably greater on the debris-covered ice than the clean ice in the 2800–5700 m a.s.l. range from 1968–~2013 in the CNR (-0.92 ±0.10 m a^{-1} vs. -0.51 ±0.10 m a^{-1}) (Fig. ~~6~~8). Similar results have been found in the eastern Pamir (Zhang et al., 2016a), the Karakoram (Gardelle et al., 2012b), the western Himalayas (Berthier et al., 2007; Frey et al., 2012) and the Mt. Everest region (Bolch et al., 2008).

Apart from debris cover, there are other features that may affect surface elevation changes, such as land- or lake-terminating glaciers, supraglacial lakes, and ice cliffs. Land-terminating glaciers with heavy debris-covers (5N225E0005, 5N225E0031, Yenong, Xiaqu, Kyagqen, Nalong, Maguolong, Yangbiegong, Cape and North Cape) experienced a mean thinning of 0.53 ±0.10 m a^{-1} from 1968–~2013, which was smaller slightly than the regional average (0.54 ± 0.10 m a^{-1}). Surface lowering of all lake-terminating glaciers (5N225E0010, 5N225E0033, Jiongla, Lepu, Daoge, Ruoguo and Star) was 0.62 ± 0.10 m a^{-1}, or higher than the regional average. Supraglacial lakes are common on most debris-covered glaciers but are not expanding as quickly as the proglacial ones (King et al., 2017; Wang et al., 2013; Ye et al., 2009). There should be a correlation between glacier elevation changes and supraglacial/proglacial lakes, because the most negative changes of lake-terminating glaciers can be attributed to termini directly affected by the expansion of supraglacial/proglacial lakes (Li et al., 2018; Neckel et al., 2017).

Although ice cliffs account for a small proportion of the total debris-covered area, they can make a disproportionate contribution to total ablation (Benn et al., 2012; Han et al., 2010). On steep slopes, heavy debris slides off leaving very fine debris on the ice cliffs. This reduces the ice albedo so the cliffs absorb more shortwave radiation, which is augmented by longwave radiation from the adjacent warm debris layers (Reid and Brock, 2014). Fig. ~~7~~ 9 shows the debris cover on Cape Glacier, its ice cliffs, and supraglacial lake. Compared to glaciers in the Kangri Karpo Mountains, subject to the same climate (Paul et al., 2015), the large debris-covered areas, exposed ice cliffs and supraglacial/proglacial lakes might be one of the reasons for the greater glacier mass loss in the CNR.

6.4 Climate change

Based on temperature data from 79 meteorological stations on the Tibetan Plateau (TP), the SE TP was the area with the least warming (Duan et al., 2015). Conversely, the MODIS land surface temperature (MODIS LST) showed that the SE TP experienced the most warming (Yang et al., 2014). The National Centers for Environmental Prediction/National Center for Atmospheric Research (NCEP/NCAR) reanalysis data results indicated a decreasing trend of average annual temperature (You et al., 2010). Similarly with precipitation, a decreasing trend in the SE TP was shown by Global Precipitation Climatology Project (GPCP) data (T. Yao et al., 2012), while a positive trend came from Chinese meteorological station annual precipitation data (Li et al., 2010). Thus, glacier changes in the CNR cannot be related directly to these summaries of climate information.

To analyse the response of glaciers in the CNR to climate change, relevant air temperature and precipitation datasets were taken from the Dataset of Daily 0.5° × 0.5° Grid-based Temperature/ Precipitation in China (V2.0) (Dataset2.0). Using the thin plate smooth spline method, and a 50 year (1961 to 2010) quality controlled observational daily temperature and precipitation data series based on 2472 gauges (http://data.cma.cn/data/cdcindex/cid/00f8a0e6c590ac15.html), Dateset2.0 was produced by the Climate Data Center, National Meteorological Information Center, China meteorological Administration for Mainland China. Previous study showed that the mean bias error of precipitation in large part gauge is between -1 mm d^{-1} and 1 mm d^{-1}. Dataset2.0 reduced the rain intensity when heavy rain or moderate rain comes. Over the light rain, it has more veracity. Dataset2.0 is exact describing the

climate characteristic of the Tibetan Plateau, the Tienshan Mountains and Tarim Basin (Zhao and Zhu, 2015). Linear regression analysis was performed in each grid for temperature and precipitation during 1961-2010. Fig. ~~8~~ 10 shows the horizontal distribution of surface temperature and precipitation changes from May to September since 1961. It is clear that increasing surface temperatures and decreasing precipitation have been dominant in the CNR in recent decades. The changes in surface temperature and precipitation were confirmed with data from the three nearest meteorological stations, Jiali (30 °40′N, 93 °17′E, 4488 m a.s.l.), Linzhi (29 °40′N, 94 °20′E, 2992 m a.s.l.) and Bomi (29 °52′N, 95 °46′E, 2736 m a.s.l.). Surface temperature at these stations increased slightly from 1961 to 2000 and then significantly after 2000, the average temperatures at the three stations after 2000 increased 0.44 ~ 0.50 ℃ than those before 2000. The trend of precipitation is not evident at the three stations and present large interannual precipitation fluctuations.

Dataset2.0 shows average precipitation decreasing by more than 40 mm per decade since 1961, resulting in less glacier accumulation. The reduced precipitation on the N slope is smaller than on the S slope, but glaciers on the N slope experienced a more intense mass loss than the S slope. This suggests the influence of precipitation is much less on glacier mass loss in the CNR. The average surface temperature increased by more than 0.2 ℃ per decade in the CNR (with a confidence level <0.05), higher than the rate of global warming (0.12 ℃ per decade, 1951–2012) (IPCC, 2013). The warming rate on the N slope is slightly larger than that on the S slope. Furthermore, a lesser warming rate was present from 1961 to 2000, becoming greater after 2000. The changes of average surface temperature are consistent with the changes of glaciers. The mean mass deficit in the 5O28 drainage basin (on the S slope) was smaller than that in the 5N22 drainage basin (on the N slope) during the investigated periods. Glacier mass loss in the CNR can be attributed to climate warming.

7 Conclusion

Based on Topographical Maps, Landsat TM/ETM+/OLI images, SRTM and TerraSAR-X/TanDEM-X acquisitions, the changes of glacier area, length, surface elevation and mass balance in the central Nyainqentanglha Range during recent decades have been estimated.

Results show that the CNR contained 715 glaciers, with a total area of 1713.42 ± 51.82 km^2 in 2016. Ice cover has diminished by 0.68% ± 0.05% a^{-1} since 1968, but the rate of glacier shrinkage has lessened during the most recent decade. Compared with the recession of mountain glaciers in western China, those in the CNR have experienced extremely strong retreat. Overall, the area covered by debris accounts for 11.9% of the whole ice cover, with the coverage decreasing in a SE-NW directions.

Significant surface lowering of glaciers has been observed since 1968, while mass losses have tended to increase. Thinning was noticeably greater on the debris-covered ice than the clean ice in the 2800–5700 m a.s.l. altitude range from 1968–~2013. Aside from debris cover, other features affecting glacier surface elevation changes include land- or lake-terminating glaciers, supraglacial lakes, and ice cliffs. Based on the Dataset of Daily 0.5 ° × 0.5 °Grid-based Temperature/Precipitation in China (V2.0), the glacier mass losses recorded in the CNR can be attributed to climate warming.

Acknowledgements. This work was supported by the fundamental programme of the National Natural Science Foundation of China (grant no. 41471067), the Ministry of Science and Technology of China (MOST) (grant no. 2013FY111400), the National Natural Science Foundation of China (grant no. 41190084, 41671057, 41671075 and 41701087), the International Partnership Programme of the Chinese Academy of Sciences (grant no.

131C11KYSB20160061) and the grant for talent introduction of Yunnan University. Landsat images are from the US Geological Survey and NASA. The GAMDAM glacier inventory was provided by A. Sakai. The first and second glacier inventories were provided by a recent MOST project (2006FY110200). The Dataset of Daily 0.5 ° × 0.5 ° Grid-based Temperature/Precipitation in China (V2.0) is from the China Meteorological Data Service Center (CMDC) in Beijing. All SAR processing was done with GAMMA SAR and interferometric processing software. We thank DLR for free access to SRTM X-band data and USGS for free access to SRTM C-band and Landsat data. ASTER GDEM and SRTM are a product of METI and NASA.

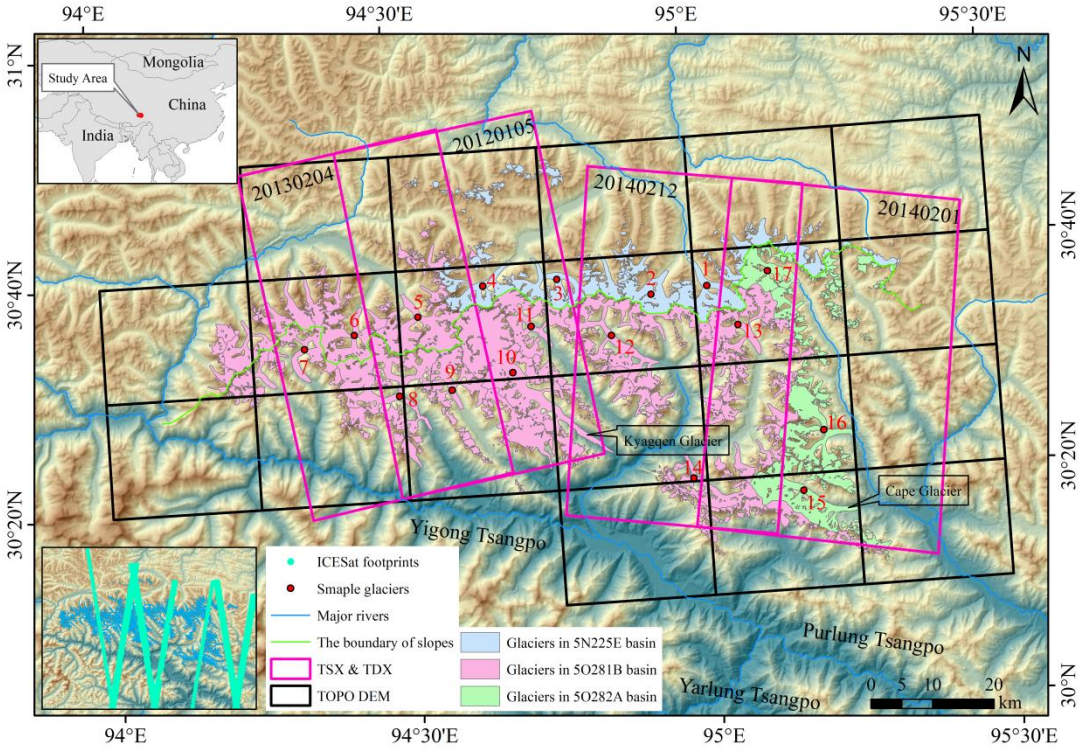

Figure 1. Study area and glacier distribution in different drainage basins. TOPO DEMs, TSX/TDX acquisitions and ICESat footprints. Numbers indicate specific sample glaciers chosen for analysis.

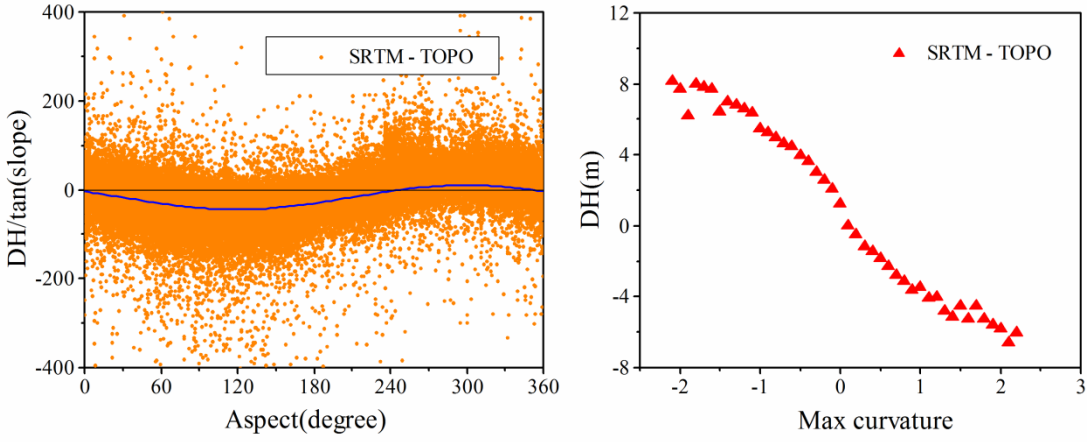

Figure 2. Scatterplots of slope standardized elevation differences vs. aspect (left) and maximum curvature (right) in the CNR.

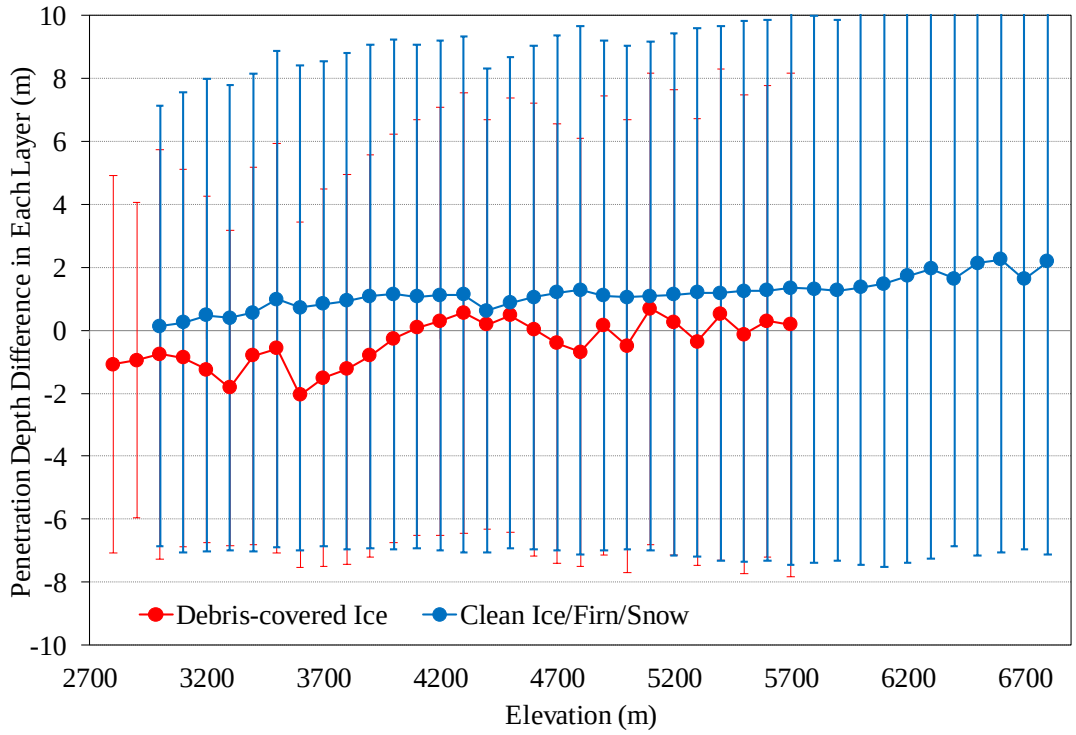

Figure 3. Penetration depth differences between SRTM C-band and X-band DEMs at each elevation bin, red indicates debris-covered ice, while blue indicates clean ice/firn/snow.

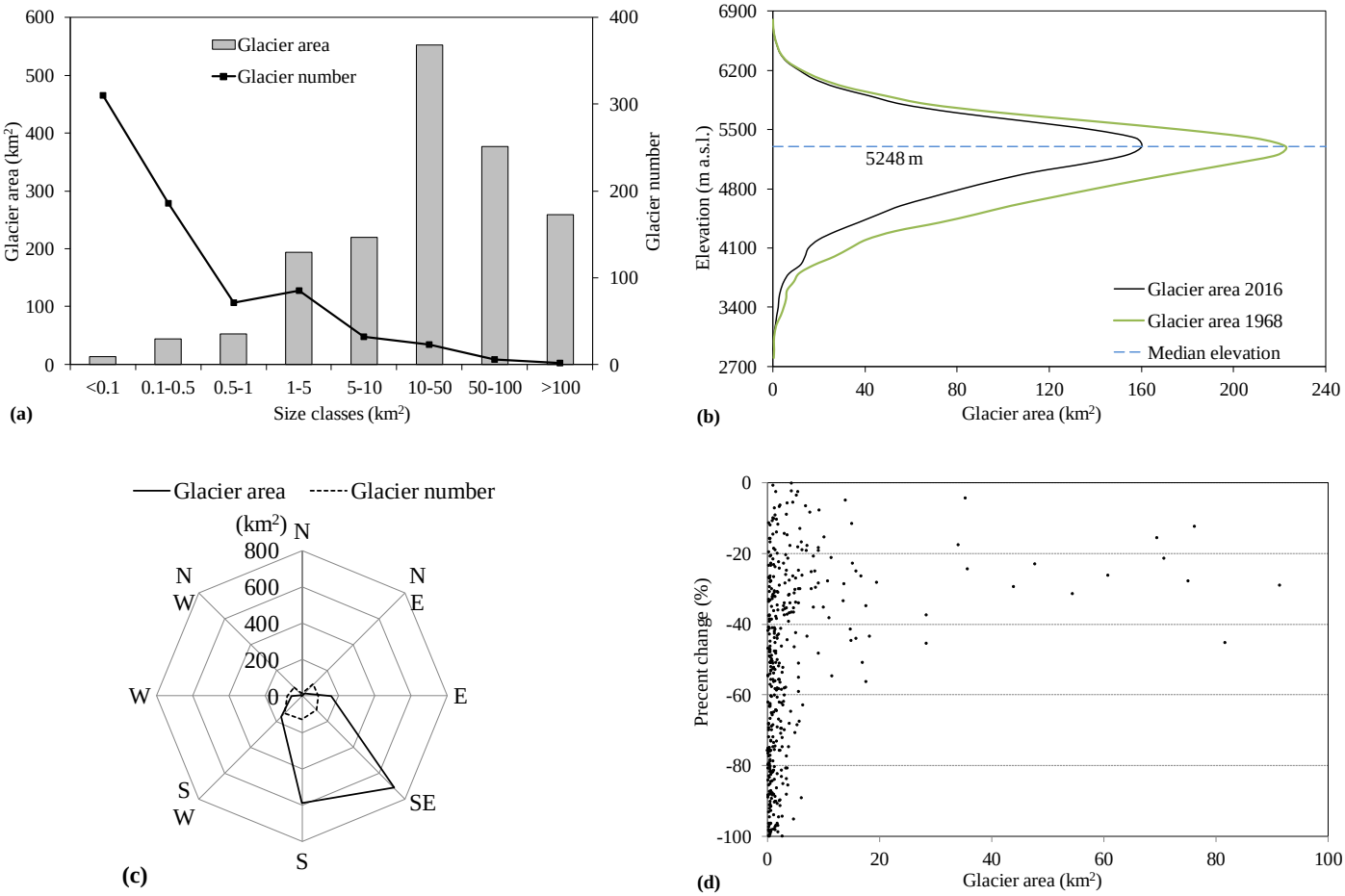

Figure ~~2~~4. Glacier distribution and change in the CNR. (a) Number and area of glaciers in different size categories. (b) Hypsography of glaciers in 1968 and 2016; the dashed line depicts the median elevation value. (c) Number and area of glaciers with different aspects. (d) Percentage change of glacier area from 1968–2016.

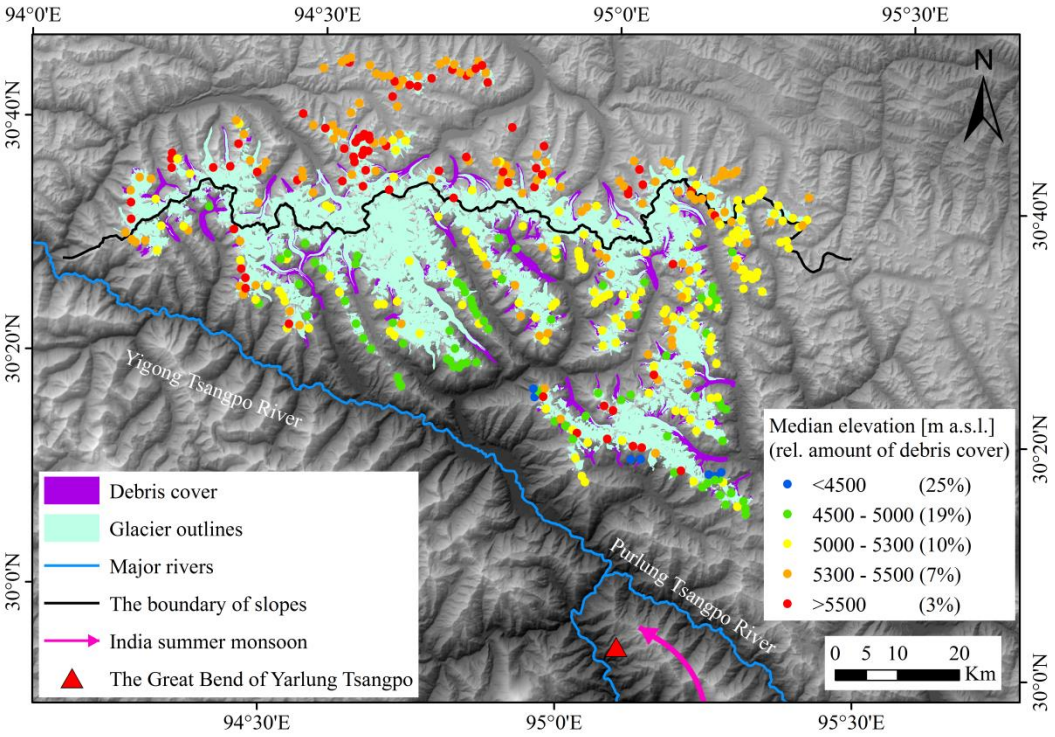

Figure ~~3~~5. Median glacier elevation and relative amount of debris cover is spatially correlated: Median elevation is increasing from southeast to northwest, whereas the debris cover (indicated by the number in brackets in the legend) is decreasing along this gradient.

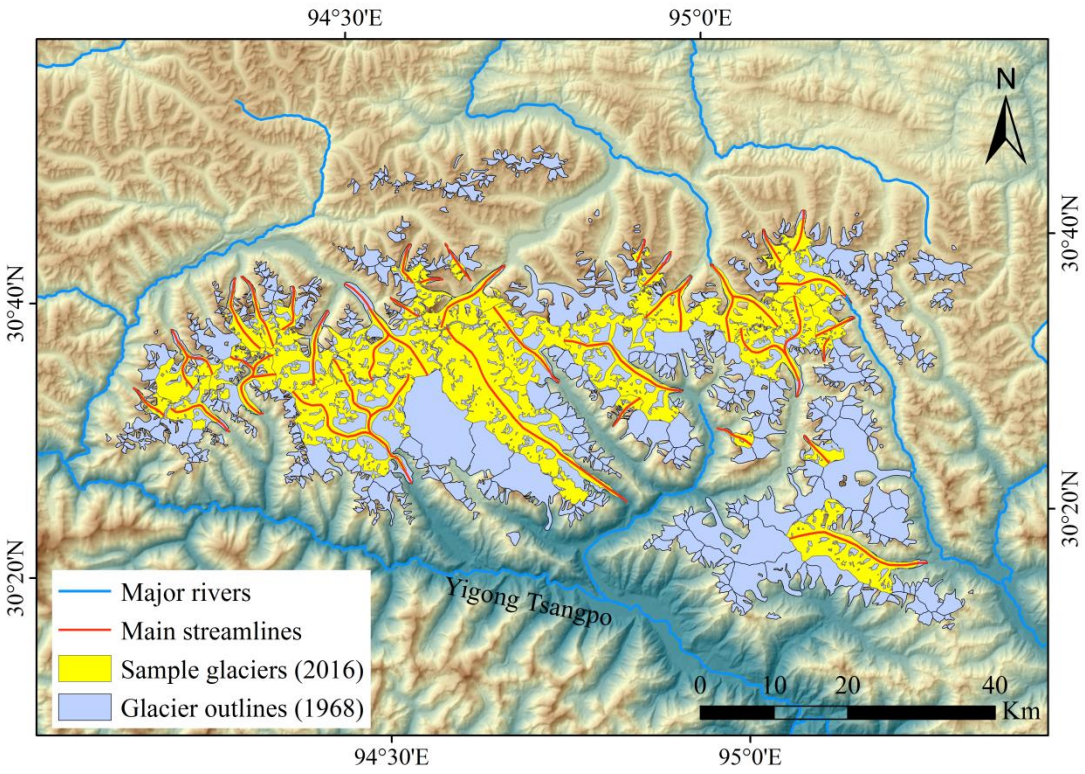

Figure ~~4~~6. The 33 sample glaciers selected for the generation of centrelines and calculation of length change.

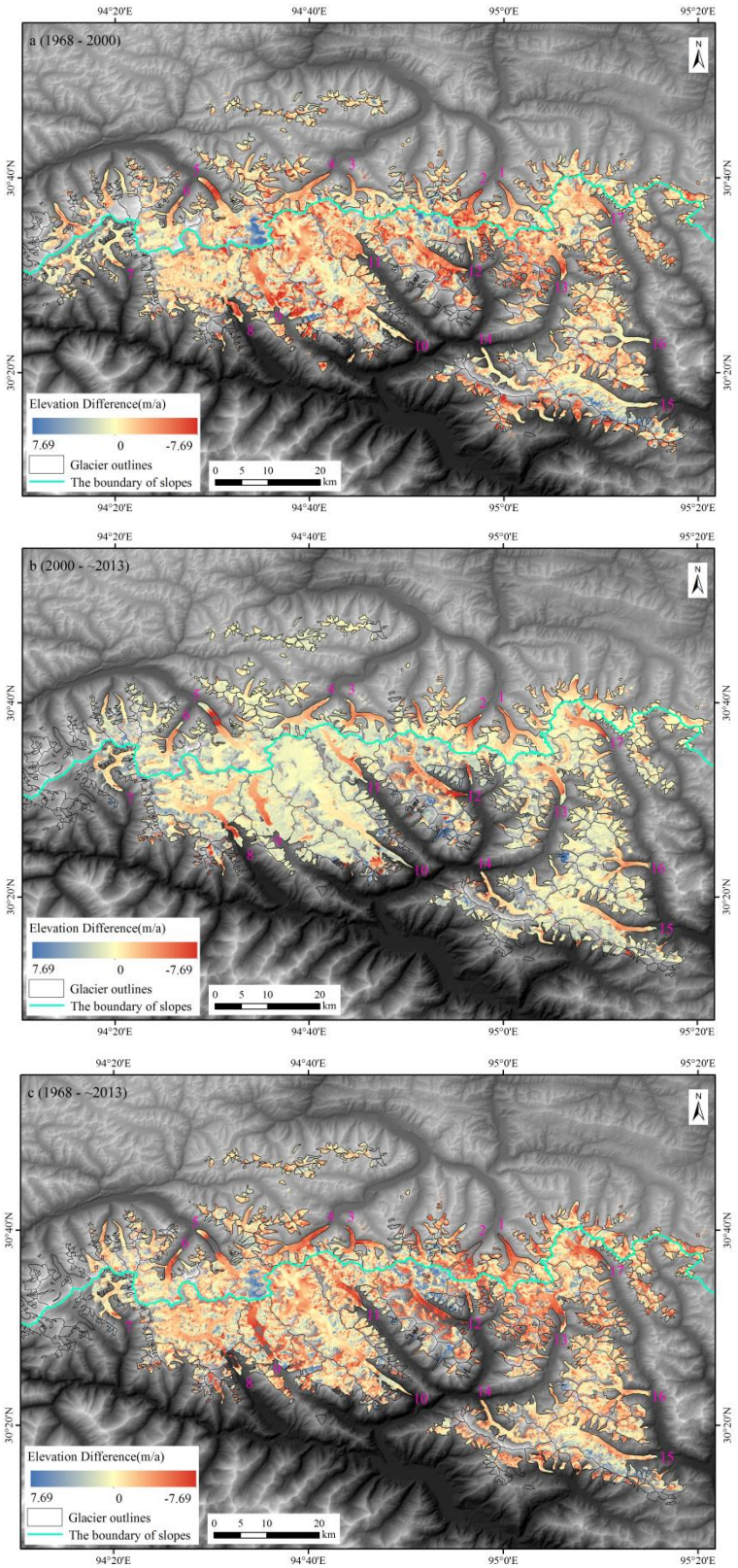

Figure ~~5~~7. Elevation changes in the CNR from 1968 to ~2013. The glacier outlines are based on the geometric union of the 1968 and 2016 glacier extents. (a) Elevation change from 1968-2000; (b) Elevation change from 2000-~2013; (c) Elevation change from 1968-~2013.

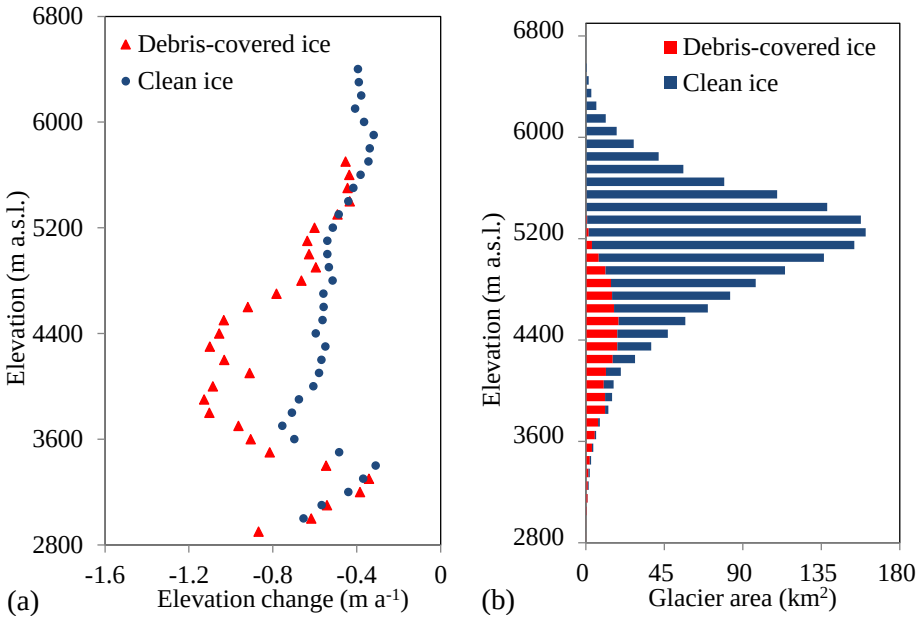

Figure ~~6~~8. Glacier elevation changes and distribution of glacier area at each 100 m interval by altitude in the CNR for clean ice and debris-covered ice from 1968 to ~2013.

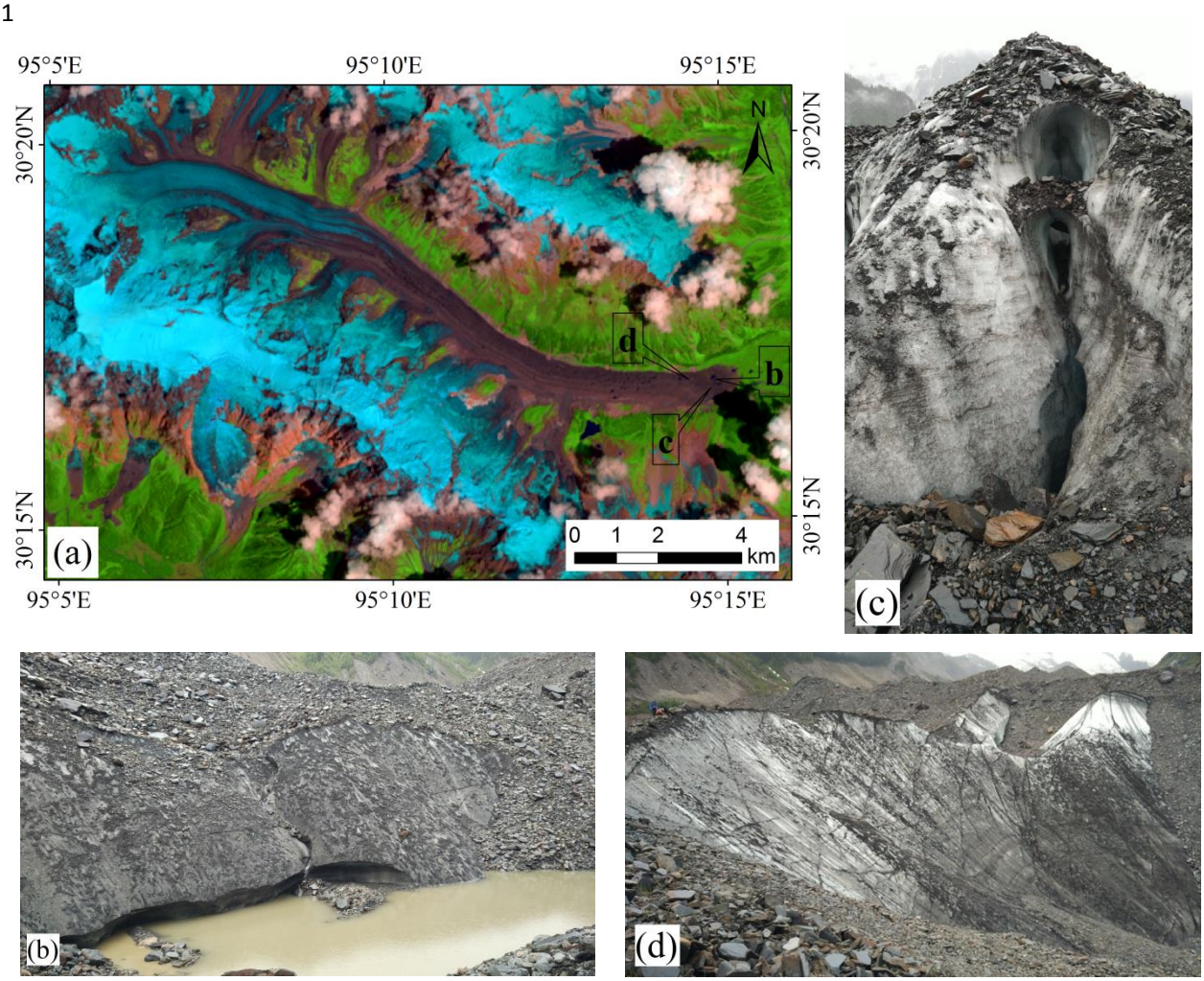

Figure ~~7~~9. The debris-covered tongue of Cape Glacier with supraglacial lakes and ice cliffs: (a) The background image is a Landsat OLI image (4 Aug 2013, RGB:743); (b) supraglacial lake; (c)&(d) ice cliffs (photos taken by K. P. Wu, 12 June 2015). The characters in tongue of Cape Glacier in panle a indicate the locations where each photo was taken.

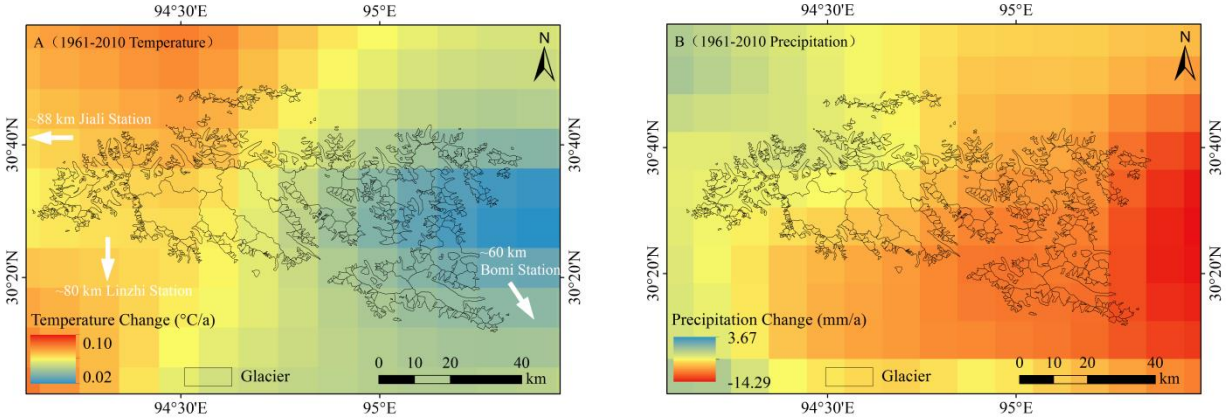

1

2 Figure ~~8~~10. The changes of temperature and precipitation (from May to September) in the CNR during
3 1961–2010: (A) Temperature; (B) precipitation.

4

5

Table 1. Overview of satellite images and data sources.

Date	Source	ID	Pixel size (m)	Utilisation
Apr 1968	Topographic Maps / TOPO DEM	H46E008018/H46E008019/ H46E008020 H46E008021/H46E008022/ H46E009017 H46E009018/H46E009019/ H46E009020 H46E009021/H46E009022/ H46E010017 H46E010018/H46E010019/ H46E010020 H46E010021/H46E010022 H46E011020 H46E011021/H46E011022	12 / 30	Glacier identification for 1968 and Estimation of glacier elevation change
11–22 Feb 2000	SRTM C-band	-	30	Estimation of glacier elevation change
4 Aug 2013	Landsat OLI	LC81350392013216LGN00	15	Glacier identification for 2016
20 Oct 2015	Landsat OLI	LC81360392015293LGN00	15	
27 Jul 2016	Landsat OLI	LC81350392016209LGN00	15	
19 Aug 2016	Landsat OLI	LC81360392016232LGN00	15	
5 Jan 2012	TSX/TDX	20120105T114457_20120105T114505	12	Estimation of glacier elevation change
4 Feb 2013	TSX/TDX	20130204T114501_20130204T114509	12	
1 Feb 2014	TSX/TDX	20140201T233757_20140201T233805	12	
12 Feb 2014	TSX/TDX	20140212T233757_20140212T233805	12	

Table 2. Specification of the bistatic TSX/TDX SAR dataset used.

Date	Relative orbit	Orbital pass	Effective perpendicular baseline (m)	Height of ambiguity (m)	Average incidence angle	Master satellite
5 Jan 2012	67	Ascending	94.5	88.2	47	TSX
4 Feb 2013	67	Ascending	126.0	-64.4	45	TSX
1 Feb 2014	59	Descending	122.0	63.3	44	TSX
12 Feb 2014	59	Descending	121.2	67.1	46	TSX

Table 3. Statistics of vertical errors between the TOPO, SRTM and TSX/TDX.

Region	Item	~~MED~~[1] AED[1] (m)	STDV[2] (m)	N[3]	SE[4] (m)	σ[5] (m)
5N225E Basin	SRTM - TOPO	-1.22	20.40	9421	0.21	1.24
	TSX/TDX - SRTM	-1.23	6.11	84762	0.02	1.23
	TSX/TDX - TOPO	-0.57	26.07	84762	0.09	0.58
5O281B Basin	SRTM - TOPO	1.13	27.51	14961	0.22	1.15
	TSX/TDX - SRTM	0.68	17.43	134579	0.05	0.68
	TSX/TDX - TOPO	-0.64	32.55	134579	0.09	0.65
5O282A Basin	SRTM - TOPO	1.27	24.79	6591	0.31	1.30
	TSX/TDX - SRTM	1.12	6.81	59281	0.03	1.12
	TSX/TDX - TOPO	0.76	32.51	59281	0.13	0.77
Total	SRTM - TOPO	-1.24	24.76	30973	0.14	1.25
	TSX/TDX - SRTM	0.79	12.09	278622	0.02	0.79
	TSX/TDX - TOPO	-0.69	30.21	278622	0.06	0.70

Note: 1 ~~MED~~ AED - ~~mean~~ average elevation difference; 2 STDV - standard deviation; 3 N - the number of considered pixels;

4 SE - standard error; 5 σ - the overall error of the derived surface elevation change.

Table 4. Glacier area changes in the CNR from 1968 to 2016.

Drainage basin	Glacier area (km^2)		Change of glacier area	
	April 1968	July 2016	Percent change from 1968-2016 (%)	Average change (% a^{-1})
5N225E	316.25±3.63	281.45±6.90	-11.00±2.07	-0.23±0.05
5O281B	1863.99±20.62	1167.01±30.71	-37.39±1.98	-0.78±0.04
5O282A	357.50±3.87	264.96±6.32	-25.89±2.07	-0.54±0.04
Total	2537.74±20.28	1713.42±51.82	-32.48±2.19	-0.68±0.05

Table 5. Length change of glaciers in the CNR. The uncertainties in glacier length in 1968 and 2016 are 6 and 7.5 m. The uncertainties in length change is 0.20 m a^{-1} during 1968 to 2016.

WGI ID	1968		2016		Length change ($m\ a^{-1}$)	Rise in terminus elevation (m)
	Length (m)	Terminus elevation (m)	Length (m)	Terminus elevation (m)		
5N225E0005	19465.11	4246	19002.16	4293	-9.64	47
5N225E0010	14915.31	4337	14010.08	4389	-18.86	52
5N225E0012	5895.97	4740	4226.54	4846	-34.78	106
5N225E0014	3354.56	5054	2791.55	5116	-11.73	62
5N225E0018	5819.22	4795	4587.67	4845	-25.66	50
5N225E0022	5201.72	4848	4164.37	4906	-21.61	58
5N225E0033	12624.73	4184	11642.76	4227	-20.46	43
5N225E0034	3074.01	5012	2457.07	5135	-12.85	123
5N225E0036	2907.52	4685	2600.69	4761	-6.39	76
5O281B0534	3355.81	4694	2240.71	4792	-23.23	98
5O281B0546	6083.60	4870	5309.17	4909	-16.13	39
5O281B0567	4742.23	4622	4525.15	4672	-4.52	50
5O281B0575	24703.52	3915	19657.25	4110	-105.13	195
5O281B0583	10774.57	4094	8506.80	4201	-47.25	107
5O281B0596	6781.61	4590	6501.30	4619	-5.84	29
5O281B0610	10804.78	4213	9773.67	4379	-21.48	166
5O281B0611	11068.81	4112	10521.56	4195	-11.40	83
5O281B0626	14162.98	4123	12339.75	4336	-37.98	213
5O281B0632	5734.49	4229	4483.55	4450	-26.06	221
5O281B0661	9636.27	3846	7707.38	4037	-40.19	191
5O281B0668	18706.15	3779	9879.99	3878	-183.88	99
5O281B0702	43458.08	3179	41656.85	3284	-37.53	105
5O281B0729	34651.63	2738	33993.28	2882	-13.72	144
5O281B0746	13687.27	3624	11756.18	3705	-40.23	81
5O281B0755	5487.93	3981	4332.47	4304	-24.07	323
5O281B0768	18371.37	3466	17789.97	3522	-12.11	56
5O281B0804	5312.66	3562	4250.48	3810	-22.13	248
5O281B0813	24408.54	3989	22164.38	4118	-46.75	129
5O281B0818	3323.90	4744	2461.76	4886	-17.96	142
5O281B0836	5143.41	4434	4331.54	4601	-16.91	167
5O282A0071	19662.20	3381	18471.66	3474	-24.80	93
5O282A0101	5840.49	4230	5277.31	4355	-11.73	125
5O282A0103	11395.90	4276	9871.65	4350	-31.76	74

Table ~~6~~5. Mean surface elevation changes and mass balance for single glaciers and different regions in the CNR from 1968 to ~2013. Glacier area is the geometric union of the 1968 and 2016 glacier areas. Mean ΔH is mean surface elevation change and mass balance is the annual mass balance. The glaciers with (*) are lake-terminating glaciers.

Region	Glacier Code (Glacier Name)	Glacier area (km^2)	1968–2000		2000–~2013		1968–~2013	
			Mean ΔH (m)	Mass balance (m w.e. a^{-1})	Mean ΔH (m)	Mass balance (m w.e. a^{-1})	Mean ΔH (m)	Mass balance (m w.e. a^{-1})
1	5N225E0005	44.46	-22.99±1.24	-0.61±0.20	-17.54±1.23	-1.15±0.31	-40.20±0.58	-0.76±0.08
2	5N225E0010*	39.05	-29.17±1.24	-0.77±0.20	-18.55±1.23	-1.21±0.31	-43.04±0.58	-0.81±0.08
3	5N225E0031	46.31	-12.10±1.24	-0.32±0.20	-11.49±1.23	-0.75±0.31	-23.43±0.58	-0.44±0.08
4	5N225E0033*	38.18	-29.81±1.24	-0.79±0.20	-10.27±1.23	-0.67±0.31	-39.96±0.58	-0.75±0.08
5N225E basin		353.38	-18.69±1.24	-0.50±0.20	-13.46±1.23	-0.88±0.31	-31.35±0.58	-0.59±0.08
5	5O281B0575 (Jiongla)*	91.53	-7.22±1.15	-0.19±0.19	-9.30±0.68	-0.61±0.17	-14.23±0.65	-0.27±0.09
6	5O281B0583 (Lepu)*	60.78	-11.20±1.15	-0.30±0.19	-8.23±0.68	-0.54±0.17	-19.75±0.65	-0.37±0.09
7	5O281B0668 (Yenong)	47.62	-2.31±1.15	-0.06±0.19	-10.76±0.68	-0.70±0.17	-13.15±0.65	-0.25±0.09
8	5O281B0702 (Xiaqu)	171.17	-14.43±1.15	-0.38±0.19	-9.57±0.68	-0.63±0.17	-23.37±0.65	-0.44±0.09
9	5O281B0714 (Daoge)*	81.67	-18.66±1.15	-0.50±0.19	-10.16±0.68	-0.66±0.17	-27.27±0.65	-0.52±0.09
10	5O281B0729 (Kyagqen)	204.67	-15.78±1.15	-0.42±0.19	-6.04±0.68	-0.40±0.17	-22.01±0.65	-0.42±0.09
11	5O281B0746 (Ruoguo)*	75.06	-23.82±1.15	-0.63±0.19	-8.13±0.68	-0.53±0.17	-31.31±0.65	-0.59±0.09
12	5O281B0768 (Nalong)	122.72	-13.06±1.15	-0.35±0.19	-16.07±0.68	-1.05±0.17	-26.37±0.65	-0.50±0.09
13	5O281B0813 (Maguolong)	75.20	-19.83±1.15	-0.53±0.19	-12.49±0.68	-0.82±0.17	-31.72±0.65	-0.60±0.09
14	5O281B0849 (Yangbiegong)	55.15	-11.84±1.15	-0.31±0.19	-12.78±0.68	-0.84±0.17	-25.86±0.65	-0.49±0.09
5O281B basin		1898.44	-15.77±1.15	-0.42±0.19	-7.78±0.68	-0.51±0.17	-23.15±0.65	-0.44±0.09
15	5O282A0071 (Cape)	77.07	-2.55±1.30	-0.07±0.21	-10.41±1.12	-0.68±0.29	-12.53±0.77	-0.24±0.11
16	5O282A0083 (North Cape)	71.78	-15.66±1.30	-0.42±0.21	-10.80±1.12	-0.71±0.29	-26.53±0.77	-0.50±0.11
17	5O282A0103 (Star)*	47.87	-17.31±1.30	-0.46±0.21	-16.64±1.12	-1.09±0.29	-32.83±0.77	-0.62±0.11
5O282A basin		372.48	-12.33±1.30	-0.33±0.21	-10.93±1.12	-0.71±0.29	-23.05±0.77	-0.44±0.11
Land-terminating glaciers		916.13	-13.92±1.25	-0.37±0.20	-10.59±0.79	-0.69±0.20	-23.95±0.70	-0.45±0.10
Lake-terminating glaciers		434.14	-18.28±1.25	-0.49±0.20	-10.97±0.79	-0.72±0.20	-27.71±0.70	-0.52±0.10
Debris-covered region		203.22	-17.64±1.25	-0.47±0.20	-25.18±0.79	-1.65±0.20	-41.36±0.70	-0.78±0.10
Clean-ice region		2421.08	-15.50±1.25	-0.41±0.20	-7.63±0.79	-0.50±0.20	-22.87±0.70	-0.43±0.10
Region of north slope		727.94	-15.01±1.24	-0.40±0.20	-10.95±1.23	-0.72±0.31	-25.17±0.58	-0.48±0.08
Region of south slope		1896.36	-15.96±1.15	-0.42±0.19	-8.55±0.68	-0.56±0.17	-24.21±0.65	-0.46±0.09
Total		2624.30	-15.69±1.25	-0.42±0.20	-9.24±0.79	-0.60±0.20	-24.48±0.70	-0.46±0.10

Table 7. A summary of glacier shrinkage in western China. Sample glaciers include Star Glacier, Maguo Lung Glacier, Ruoguo Glacier, Jiangpu Glacier, Nalong Glacier, Cape Glacier, North Cape Glacier and Yangbiegong Glacier.

Region		Period	Absolute ice loss (km^2)	Area change (%)	Average change (% a^{-1})	Reference
Altay		1960 – 2009	-104.61	-36.91	-0.75	(X. Yao et al., 2012)
Kangri Karpo		1980 – 2015	-679.50	-24.91	-0.71	(Wu et al., 2018)
Tian Shan		1960 – 2010	–	-11.5	-0.22	(Wang et al., 2011)
eastern Pamir		1963 – 2009	-248.70	-10.80	-0.25	(Zhang et al., 2016)
western Kunlun		1970 – 2010	-95.06	-3.37	-0.09	(Bao et al., 2015)
Qilian Mountain		1956 – 2005	-417.15	-20.70	-0.47	(Sun et al., 2015)
the interior area of the TP		1970 – 2009	-766.65	-9.54	-0.26	(Wei et al., 2014)
Everest		1976 – 2006	-501.91	-15.63	-0.56	(Nie et al., 2010)
Gangga Mountain		1966 – 2009	-29.20	-11.33	-0.28	(Pan et al., 2012)
the CNR	Whole Range	1968 – 2016	-824.32	-32.5	-0.68	This study
	Sample Glaciers*	1968 – 1999	-257.19	-38.23	-1.23	(Ji et al., 2014, 2015)
		1999 – 2011	-40.84	-9.83	-0.82	

References

Arendt, A., Bliss, A., Bolch, T., Cogley, J.G., Gardner, A.S., Hagen, J.-O., Hock, R., Huss, M., Kaser, G., Kienholz, C., Pfeffer, W., Moholdt, G., Paul, F., Radic, V., Andreassen, L., Bajracharya, S., Barrand, N.E., Beedle, M., Berthier, E., Bhambri, R., Brown, I., Burgess, E., Burgess, D., Cawkwell, F., Chinn, T., Copland, L., Davies, B., de Angelis, H., Dolgova, E., Earl, L., Filbert, K., Forester, R., Fountain, A., Frey, H., Giffen, B., Glasser, N., Guo, W.Q., Gurney, S., Hagg, W., Hall, D., Haritashya, U.K., Hartmann, G., Helm, C., Herreid, S., Howat, I., Kapustin, G., Khromova, T., König, M., Kohler, J., Kriegel, D., Kutuzov, S., Lavrentiev, I., LeBris, R., Liu, S.Y., Lund, J., Manley, W., Marti, R., Mayer, C., Miles, E.S., Li, X., Menounos, B., Mercer, A., Mölg, N., Mool, P., Nosenko, G., Negrete, A., Nuimura, T., Nuth, C., Pettersson, R., Racoviteanu, A., Ranzi, R., Rastner, P., Rau, F., Raup, B., Rich, J., Rott, H., Sakai, A., Schneider, C., Seliverstov, Y., Sharp, M., Sigurðsson, O., Stokes, C., Way, R.G., Wheate, R., Winsvold, S., Wolken, G., Wyatt, F. & Zheltyhina, N. (2015). *Randolph glacier inventory – a dataset of global glacier outlines. Version 5.0.* Boulder, CO, University of Colorado. National Snow and Ice Data Center (NSIDC). Global Land Ice Measurements from Space (GLIMS), digital media, 63 pp. (www.glims.org/RGI/00_rgi50_TechnicalNote.pdf.)

Bao, W., Liu, S., Wei, J. & Guo, W. (2015). Glacier changes during the past 40 years in the West Kunlun Shan. *J. Mtn Sci.*, **12**(2), March, 344–357. (doi: 10.1007/s11629-014-3220-0.)

Benn, D.I. & Lehmkuhl, F. (2000). Mass balance and equilibrium-line altitudes of glaciers in high-mountain environments. *Quat. Int.*, **65–66**, 1 April, 15–29. (doi: 10.1016/S1040-6182(99)00034-8.)

Benn, D.I., Bolch, T., Hands, K., Gulley, J., Luckman, A., Nicholson, L.I., Quincey, D., Thompson, S., Toumi, R. & Wiseman, S. (2012). Response of debris-covered glaciers in the Mount Everest region to recent warming, and implications for outburst flood hazards. *Earth-Sci. Rev.*, **114**(1-2), August, 156–174. (doi: 10.1016/j.earscirev.2012.03.008.)

Berthier, E., Arnaud, Y., Vincent, C. & Rémy, F. (2006). Biases of SRTM in high-mountain areas: implications for the monitoring of glacier volume changes. *Geophys. Res. Lett.*, **33**(8), 25 April, L08502. (doi: 10.1029/2006GL025862.)

Berthier, E., Arnaud, Y., Kumar, R., Ahmad, S., Wagnon, P. & Chevallier, P. (2007). Remote sensing estimates of glacier mass balances in the Himachal Pradesh (Western Himalaya, India). *Rem. Sens. Environ.*, **108**(3), 15 June, 327–338. (doi: 10.1016/j.rse.2006.11.017.)

Berthier, E., Larsen, C., Durkin, W. J., Willis, M. J., and Pritchard, M. E. (2018): Brief communication: Unabated wastage of the Juneau and Stikine icefields (southeast Alaska) in the early 21st century, The Cryosphere, 12, 1523-1530,https://doi.org/10.5194/tc-12-1523-2018.

Berthier, E., Schiefer, E., Clarke, G.K.C., Menounos, B. & Rémy, F. (2010). Contribution of Alaskan glaciers to sea-level rise derived from satellite imagery. *Nature Geosci.*, **3**(2), February, 92–95. (doi: 10.1038/ngeo737.)

Bolch, T., Buchroithner, M., Pieczonka, T. & Kunert, A. (2008). Planimetric and volumetric glacier changes in the Khumbu Himal, Nepal, since 1962 using Corona, Landsat TM and ASTER data. *J. Glaciol.*, **54**(187), 592–600. (doi: 10.3189/002214308786570782.)

Bolch, T., Menounos, B. & Wheate, R. (2010a). Landsat-based inventory of glaciers in western Canada, 1985–2005. *Rem. Sens. Environ.*, **114**(1), 127–137. (doi: 10.1016/j.rse.2009.08.015.)

Bolch, T., Yao, T., Kang, S., Buchroithner, M.F., Scherer, D., Maussion, F., Huintjes, E. & Schneider, C. (2010b). A glacier inventory for the western Nyainqentanglha Range and Nam Co Basin, Tibet, and glacier changes 1976–2009. *Cryosphere (TC)*, **4**(3), 29 September, 419–433. (doi: 10.5194/tc-4-419-2010.)

Bolch, T., Pieczonka, T. & Benn, D.I. (2011). Multi-decadal mass loss of glaciers in the Everest area (Nepal Himalaya) derived from stereo imagery. Cryosphere (TC), 5(2), 20 April, 349–358. (doi: 10.5194/tc-5-349-2011.)

Braithwaite, R.J. & Raper, S.C.B. (2009). Estimating equilibrium line altitude (ELA) from glacier inventory data. *Ann.*

Glaciol., **50**(53), 127–132. (doi: 10.3189/172756410790595930.)

Brun, F., Berthier, E., Wagnon, P., Kääb, A. & Treichler, D. (2017). A spatially resolved estimate of High Mountain Asia glacier mass balances from 2000 to 2016. *Nature Geosci.*, **10**(9), September, 668–673. (doi: 10.1038/ngeo2999.)

Chinese National Standard. (2008). [*Compilation specifications for national fundamental scale maps. Part 1: Compilation specifications for 1:25000/1:50000/1:100000 topographic maps.]* Beijing, General Administration of Quality Supervision, Inspection and Quarantine. (GB/T 12343.1-2008.) (In Chinese)

Cuffey, K.M. & Paterson, W.S.B. (2010). *The physics of glaciers. Fourth edition*. Amsterdam, etc., Elsevier. Butterworth-Heinemann, 488 pp.

Davis, C.H. & Poznyak, V.I. (1993). The depth of penetration in Antarctic firn at 10 GHz. *IEEE Trans. Geosci. Rem. Sens.*, **31**(5), September, 1107–1111. (doi: 10.1109/36.263784.)

Duan, J., Li, L. & Fang, Y. (2015). Seasonal spatial heterogeneity of warming rates on the Tibetan Plateau over the past 30 years. *Sci. Rep.*, **5**, 26 June, 11725. (doi: 10.1038/srep11725.)

Frey, H., Paul, F. & Strozzi, T. (2012). Compilation of a glacier inventory for the western Himalayas from satellite data: methods challenges and results. *Rem. Sens. Environ.*, **124**, September, 832–843. (doi: 10.1016/j.rse.2012.06.020.)

Gardelle, J., Berthier, E. & Arnaud, Y. (2012a). Impact of resolution and radar penetration on glacier elevation changes computed from DEM differencing. [Correspondence.] *J. Glaciol.*, **58**(208), 419–422. (doi: 10.3189/2012JoG11J175.)

Gardelle, J., Berthier, E. & Arnaud, Y. (2012b). Slight mass gain of Karakoram glaciers in the early twenty-first century. *Nature Geosci.*, **5**(5), May, 322–325. (doi: 10.1038/ngeo1450.)

Gardelle, J., Berthier, E., Arnaud, Y. & Kääb, A. (2013). Region-wide glacier mass balances over the Pamir–Karakoram–Himalaya during 1999–2011. *Cryosphere (TC)*, **7**(4), 9 August, 1263–1286. (doi: 10.5194/tc-7-1263-2013.)

Gardner, A.S., Moholdt, G., Cogley, J.G., Wouters, B., Arendt, A.A., Wahr, J., Berthier, E., Hock, R., Pfeffer, W.T., Kaser, G., Ligtenberg, S.R.M., Bolch, T., Sharp, M.J., Hagen, J.O., van den Broeke, M.R. & Paul, F. (2013). A reconciled estimate of glacier contributions to sea level rise: 2003 to 2009. *Science*, **340**(6134), 17 May, 852–857. (doi: 10.1126/science.1234532.)

Guo, W., Liu, S., Xu, J., Wu, L., Shangguan, D., Yao, X., Wei, J., Bao, W., Yu, P., Liu, Q. & Jiang, Z. (2015). The second Chinese glacier inventory: data, methods, and results. *J. Glaciol.*, **61**(226), 357–372. (doi: 10.3189/2015JoG14J209.)

Han, H., Wang, J., Wei, J. & Liu, S. (2010). Backwasting rate on debris-covered Koxkar glacier, Tuomuer mountain, China. *J. Glaciol.*, **56**(196), 287–296. (doi: 10.3189/002214310791968430.)

Huss, M. (2013). Density assumptions for converting geodetic glacier volume change to mass change. *Cryosphere (TC)*, **7**(3), 28 May, 877–887. (doi: 10.5194/tc-7-877-2013.)

Immerzeel, W.W., van Beek, L.P.H. & Bierkens, M.F.P. (2010). Climate change will affect the Asian water towers. *Science*, **328**(5984), 11 June, 1382–1385. (doi: 10.1126/science.1183188.)

IPCC. (2013). Climate change 2013: *The physical science basis. Contribution of Working Group I to the Fifth Assessment Report of the Intergovernmental Panel on Climate Change.* Cambridge, UK and New York, NY, USA, Cambridge University Press, 1535 pp. (doi: 10.1017/CBO9781107415324.)

Jaber, W.A., Floricioiu, D., Rott, H. & Eineder, M. (2012). Dynamics of fast glaciers in the Patagonia Icefields derived from TerraSAR-X and TanDEM-X data. *2012 IEEE International Geoscience & Remote Sensing Symposium, 22–27 July 2012, Munich, Germany. Proceedings*, New York, NY, Institute of Electrical and Electronics Engineers, 3226–3229. (doi: 10.1109/IGARSS.2012.6350737.)

Ji, Q., Yang, T. & Li, X. (2014). [Study on relationship between glacier retreat and climate change in the eastern

Nyainqentanglha in the past 40 years.] *[Res. Soil Water Conserv.]*, **21**(2), 306–310. (In Chinese with English summary)

Ji, Q., Yang, T. & Li, X. (2015). [Relationship between glacier retreat and climate change in eastern Nyainqentanglha in the past 40 years.] *[J. Arid Land Resour. Environ.]*, **29**(2), 166–171. (In Chinese with English summary)

Kääb, A. (2005). Combination of SRTM3 and repeat ASTER data for deriving alpine glacier flow velocities in the Bhutan Himalaya. *Rem. Sens. Environ.*, **94**(4), 28 February, 463–474. (doi: 10.1016/j.rse.2004.11.003.)

Kääb, A., Berthier, E., Nuth, C., Gardelle, J. & Arnaud, Y. (2012). Contrasting patterns of early twenty-first-century glacier mass change in the Himalayas. *Nature*, **488**(7412), 23 August, 495–498. (doi: 10.1038/nature11324.)

Kääb, A., Treichler, D., Nuth, C. & Berthier, E. (2015). Contending estimates of 2003–2008 glacier mass balance over the Pamir–Karakoram–Himalaya. [Brief Communication.] *Cryosphere (TC)*, **9**(2), 19 March, 557–564. (doi: 10.5194/tc-9-557-2015.)

Ke, L., Ding, X. & Song, C. (2015). Heterogeneous changes of glaciers over the western Kunlun Mountains based on ICESat and Landsat-8 derived glacier inventory. *Rem. Sens. Environ.*, **168**, October, 13–23. (doi: 10.1016/j.rse.2015.06.019.)

Ke, L., Ding, X., Zhang, L., Hu, J., Shum, C.K. & Lu, Z. (2016). Compiling a new glacier inventory for southeastern Qinghai–Tibet Plateau from Landsat and PALSAR data. *J. Glaciol.*, **62**(233), June, 579–592. (doi: 10.1017/jog.2016.58.)

Kienholz, C., Rich, J.L., Arendt, A.A. & Hock, R. (2014). A new method for deriving glacier centerlines applied to glaciers in Alaska and northwest Canada. *Cryosphere (TC)*, **8**(2), 26 March, 503–519. (doi: 10.5194/tc-8-503-2014.)

King, O., Quincey, D.J., Carrivick, J.L. & Rowan, A.V. (2017). Spatial variability in mass loss of glaciers in the Everest region, central Himalayas, between 2000 and 2015. *Cryosphere (TC)*, **11**(1), 3 February, 407–426. (doi: 10.5194/tc-11-407-2017.)

Koblet, T., Gärtner-Roer, I., Zemp, M., Jansson, P., Thee, P., Haeberli, W. & Homlund, P. (2010). Reanalysis of multi-temporal aerial images of Storglaciären, Sweden (1959–99). Part 1: Determination of length, area, and volume changes. *Cryosphere (TC)*, **4**(3), 8 September, 333–343. (doi: 10.5194/tc-4-333-2010.)

Krieger, G., Moreira, A., Fiedler, H., Hajnsek, I., Werner, M., Younis, M. & Zink, M. (2007). TanDEM-X: a satellite formation for high-resolution SAR interferometry. *IEEE Trans. Geosci. Rem. Sens.*, **45**(11), November, 3317–3341. (doi: 10.1109/TGRS.2007.900693.)

Kubanek, J., Westerhaus, M., Schenk, A., Aisyah, N., Brotopuspito, K.S. & Heck, B. (2015). Volumetric change quantification of the 2010 Merapi eruption using TanDEM-X InSAR. *Rem. Sens. Environ.*, **164**, July, 16–25. (doi: 10.1016/j.rse.2015.02.027.)

Langley, K., Hamran, S.-E., Høgda, K.A., Storvold, R., Brandt, O., Kohler, J. & Hagen, J.O. (2008). From glacier facies to SAR backscatter zones via GPR. *IEEE Trans. Geosci. Rem. Sens.*, **46**(9), September, 2506–2516. (doi: 10.1109/TGRS.2008.918648.)

Le Bris, R. & Paul, F. (2013). An automatic method to create flow lines for determination of glacier length: a pilot study with Alaskan glaciers. *Comput. Geosci.*, **52**, March, 234–245. (doi: 10.1016/j.cageo.2012.10.014.)

Li, G. & Lin, H. (2017). Recent decadal glacier mass balances over the Western Nyaingentanglha Mountains and the increase in their melting contribution to Nam Co Lake measured by differential bistatic SAR interferometry. *Global Planet. Change*, **149**, February, 177–190. (doi: 10.1016/j.gloplacha.2016.12.018.)

Li, J., Zheng, B. & Yang, X. (1986). *[The glaciers of Xizang (Tibet).]* Beijing, Science Press. Chinese Academy of Sciences, ix + 328 pp. ([Scientific Expedition to the Qinghai–Xizang Plateau].) (In Chinese with English table of contents)

Li, X., Yang, T.-B. & Ji, Q. (2014). [Study on glacier variations in the Gangrigabu Range.] *[Res. Soil Water Conserv.]*,

21(4), 233–237. (In Chinese with English summary)

Li, G., Lin, H. & Ye, Q. (2018). Heterogeneous decadal glacier downwasting at the Mt. Everest (Qomolangma) from 2000 to similar to 2012 based on multi-baseline bistatic SAR interferometry. *Rem. Sens. Environ.*, **206**, March, 336–349. (doi: 10.1016/j.rse.2017.12.032.)

Li, L., Yang, S., Wang, Z., Zhu, X. & Tang, H. (2010). Evidence of warming and wetting climate over the Qinghai–Tibet Plateau. *Arct. Ant. Alp. Res.*, **42**(4), November, 449–457. (doi: 10.1657/1938-4246-42.4.449.)

Li, Z., Xing, Q., Liu, S., Zhou, J. & Huang, L. (2012). Monitoring thickness and volume changes of the Dongkemadi ice field on the Qinghai–Tibetan Plateau (1969–2000) using Shuttle Radar Topography Mission and map data. *Int. J. Digital Earth*, **5**(6), June, 516-532. (doi: 10.1080/17538947.2011.594099.)

Li, X., Cheng, G., Jin, H., Kang, E., Che, T., Jin, R., Wu, L., Nan, Z., Wang, J. & Shen, Y. (2008). Cryospheric change in China. *Global Planet. Change*, **62**(3–4), June, 210–218. (doi: 10.1016/j.gloplacha.2008.02.001.)

Liu, S., Zhong, Y., Liu, Q., Sun, M., Wang, X., Wei, J. & Yao, X., *eds.* (2017). *[Climate change impacts and risks. The research of climate change impacts and risks on glacier.]* Beijing, Science Press. (In Chinese)

Loibl, D., Lehmkuhl, F., Grießinger, J. (2014). Reconstructing glacier retreat since the Little Ice Age in SE Tibet by glacier mapping and equilibrium line altitude calculation. *Geomorphology*, 214, 22–39.

Mi, D., Xie, Z., Luo, X., Feng, Q., Ma, M. & Jin, D. (2002). *[Glacier inventory of China XI. the Ganga drainage basin. XII. Indus drainage basin.]* Xi'an, Xi'an Cartographic Publishing House. Lanzhou Institute of Glaciology and Geocryology, 552 pp. (In Chinese)

Neckel, N., Braun, A., Kropáček, J. & Hochschild, V. (2013). Recent mass balance of the Purogangri ice cap, central Tibetan Plateau, by means of differential X-band SAR interferometry. *Cryosphere (TC)*, **7**(5), 24 October, 1623–1633. (doi: 10.5194/tc-7-1623-2013.)

Neckel, N., Kropáček, J., Bolch, T. & Hochschild, V. (2014). Glacier mass changes on the Tibetan Plateau 2003–2009 derived from ICESat laser altimetry measurements. *Environ. Res. Lett.*, **9**(1), January, 014009. (doi: 10.1088/1748-9326/9/1/014009.)

Neckel, N., Loibl, D. & Rankl, M. (2017). Recent slowdown and thinning of debris-covered glaciers in south-eastern Tibet. *Earth Planet. Sci. Lett.*, **464**, April, 95–102. (doi: 10.1016/j.epsl.2017.02.008.)

Neelmeijer, J., Motagh, M., Bookhagen, B. (2017): High-resolution digital elevation models from single-pass TanDEM-X interferometry over mountainuous region: a case study of Inylchek Glacier, Central Asia. ISPRS J. Photogramm. Remote Sens. 130, 108–121. http://dx.doi.org/10.1016/j.isprsjprs.2017.05.011.

Nie, Y., Zhang, Y., Liu, L. & Zhang, J. (2010). Glacial change in the vicinity of Mt. Qomolangma (Everest), central high Himalayas since 1976. *J. Geogr. Sci.*, **20**(5), October, 667–686. (doi: 10.1007/s11442-010-0803-8.)

Nuimura, T., Sakai, A., Taniguchi, K., Nagai, H., Lamsal, D., Tsutaki, S., Kozawa, A., Hoshina, Y., Takenaka, S., Omiya, S., Tsunematsu, K., Tshering, P. & Fujita, K. (2015). The GAMDAM glacier inventory: a quality-controlled inventory of Asian glaciers. *Cryosphere (TC)*, **9**(3), 6 May, 849–864. (doi: 10.5194/tc-9-849-2015.)

Nuth, C. & Kääb, A. (2011). Co-registration and bias corrections of satellite elevation data sets for quantifying glacier thickness change. *Cryosphere (TC)*, **5**(1), 29 March, 271–290. (doi: 10.5194/tc-5-271-2011.)

Oerlemans, J. (1994). Quantifying global warming from the retreat of glaciers. *Science*, **264**(5156), 8 April, 243–245. (doi: 10.1126/science.264.5156.243.)

Pan, B.T., Zhang, G.L., Wang, J., Cao, B., Geng, H.P., Wang, J., Zhang, C. & Ji, Y.P. (2012). Glacier changes from 1966–2009 in the Gongga Mountains, on the south-eastern margin of the Qinghai–Tibetan Plateau and their climatic forcing. *Cryosphere (TC)*, **6**(5), 2 October, 1087–1101. (doi: 10.5194/tc-6-1087-2012.)

Paul, F., Huggel, C., Kääb, A., Kellenberger, T. & Maisch, M. (2003). Comparison of TM-derived glacier areas with higher resolution data sets. *EARSeL eProc.*, **2**(1), 15–21. (www.eproceedings.org/static/vol02_1/02_1_paul1.pdf.)

Paul, F., Barry, R.G., Cogley, J.G., Frey, H., Haeberli, W., Ohmura, A., Ommanney, C.S.L., Raup, B., Rivera, A. & Zemp, M. (2009). Recommendations for the compilation of glacier inventory data from digital sources. *Ann. Glaciol.*, **50**(53), 119–126. (doi: 10.3189/172756410790595778.)

Paul, F., Bolch, T., Kääb, A., Nagler, T., Nuth, C., Scharrer, K., Shepherd, A., Strozzi, T., Ticconi, F., Bhambri, R., Berthier, E., Bevan, S., Gourmelen, N., Heid, T., Jeong, S., Kunz, M., Lauknes, T.R., Luckman, A., Merryman Boncori, J.P., Moholdt, G., Muir, A., Neelmeijer, J., Rankl, M., VanLooy, J. & van Niel, T. (2015). The glaciers climate change initiative: methods for creating glacier area, elevation change and velocity products. *Rem. Sens. Environ.*, **162**, 1 June, 408–426. (doi: 10.1016/j.rse.2013.07.043.)

Pellicciotti, F., Stephan, C., Miles, E., Herreid, S., Immerzeel, W.W. & Bolch, T. (2015). Mass-balance changes of the debris-covered glaciers in the Langtang Himal, Nepal, between 1974 and 1999. *J. Glaciol.*, **61**(226), 373–386. (doi: 10.3189/2015JoG13J237.)

Pfeffer, W.T., Arendt, A.A., Bliss, A., Bolch, T., Cogley, J.G., Gardner, A.S., Hagen, J.-O., Hock, R., Kaser, G., Kienholz, C., Miles, E.S., Moholdt, G., Mölg, N., Paul, F., Radic, V., Rastner, P., Raup, B.H., Rich, J., Sharp, M.J. & the Randolph Consortium. (2014). The Randolph Glacier Inventory: a globally complete inventory of glaciers. *J. Glaciol.*, **60**(221), 537–552. (doi: 10.3189/2014JoG13J176.)

Pieczonka, T., Bolch, T., Wei, J. & Liu, S. (2013). Heterogeneous mass loss of glaciers in the Aksu-Tarim catchment (central Tien Shan) revealed by 1976 KH-9 Hexagon and 2009 SPOT-5 stereo imagery. *Rem. Sens. Environ.*, **130**, 15 March, 233–244. (doi: 10.1016/j.rse.2012.11.020.)

Pu, J. (2001). *[Glacier Inventory of China IX. The Lancang river. X. The Nujiang river.]* Xi'an, Xi'an Cartographic Publishing House, 179 pp. (In Chinese.)

Rabus, B., Eineder, M., Roth, A. & Bamler, R. (2003). The Shuttle radar topography mission: a new class of digital elevation models acquired by spaceborne radar. ISPRS J. Photogram. *Rem. Sens.*, **57**(4), February, 241–262. (doi: 10.1016/S0924-2716(02)00124-7.)

Racoviteanu, A.E., Williams, M.W. & Barry, R.G. (2008). Optical remote sensing of glacier characteristics: a review with focus on the Himalaya. *Sensors*, **8**(5), May, 3355–3383. (doi: 10.3390/s8053355.)

Racoviteanu, A.E., Paul, F., Raup, B.H., Khalsa, S.J.S. & Armstrong, R. (2009). Challenges and recommendations in mapping of glacier parameters from space: results of the 2008 Global Land Ice Measurements from Space (GLIMS) workshop, Boulder, Colorado, USA. *Ann. Glaciol.*, **50**(53), 53–69. (doi: 10.3189/172756410790595804.)

Reid, T.D. & Brock, B.W. (2014). Assessing ice-cliff backwasting and its contribution to total ablation of debris-covered Miage glacier, Mont Blanc massif, Italy. *J. Glaciol.*, **60**(219), 3–13. (doi: 10.3189/2013JoG13J045.)

Rignot E, Echelmeyer K and Krabill W (2001): Penetration depth of interferometric synthetic-aperture radar signals in snow and ice. Geophys. Res. Lett., 28(18), 3501– 3504. doi: 10.1029/2000GL012484.

Scherler, D., Bookhagen, B. & Strecker, M.R. (2011). Spatially variable response of Himalayan glaciers to climate change affected by debris cover. *Nature Geosci.*, **4**(3), March, 156–159. (doi: 10.1038/ngeo1068.)

Schiefer, E., Menounos, B. & Wheate, R. (2008). An inventory and morphometric analysis of British Columbia glaciers, Canada. *J. Glaciol.*, **54**(186), 551–560. (doi: 10.3189/002214308785836995.)

Shangguan, D., Liu Shiyin, Ding Yongjian, Zhang Yingsong, Li Jing, Li Xiangying & Wu Zhen. (2010). Changes in the elevation and extent of two glaciers along the Yanglonghe River, Qilian Shan, China. *J. Glaciol.*, **56**(196), 309–317. (doi: 10.3189/002214310791968566.)

Shangguan, D., Liu, S., Ding, Y., Wu, L., Deng, W., Guo, W., Wang, Y., Xun, J., Yao, X., Guo, Z. & Zhu, W. (2014). Glacier changes in the Koshi River basin, central Himalaya, from 1976 to 2009, derived from remote-sensing imagery. *Ann. Glaciol.*, **55**(66), 61–68. (doi: 10.3189/2014AoG66A057.)

Shi, Y. & Liu, S. (2000). Estimation on the response of glaciers in China to the global warming in the 21st century. *Chin. Sci. Bull.*, **45**(7), April, 668–672. (doi: 10.1007/BF02886048.)

Shi, Y., Huang, M. & Ren, B., *eds*. (1988). *[An introduction to the glaciers in China.]* Beijing, Science Press, 243 pp. (In Chinese)

Shi, Y., Huang, M., Yao, T. & He, Y., *eds*. (2008). *Glaciers and related environments in China*. Beijing, Science Press, xv + 553 pp.

Sun, M., Liu, S., Yao, X., Guo, W. & Xu, J. (2015). [Glacier changes in the Qilian Mountains in the past half century: based on the revised First and Second Chinese Glacier Inventory.] *Acta Geogr. Sinica*, **70**(9), September, 1402–1414. (Chinese with English summary)

Surdyk, S. (2002). Using microwave brightness temperature to detect short-term surface air temperature changes in Antarctica: an analytical approach. *Rem. Sens. Environ.*, **80**(2), May, 256–271. (doi: 10.1016/S0034-4257(01)00308-X.)

Vijay, S.; Braun, M. Elevation Change Rates of Glaciers in the Lahaul-Spiti (Western Himalaya, India) during 2000–2012 and 2012–2013 (2016): Remote Sens. 2016, 8, 1038.

Wang, S., Zhang, M., Li, Z., Wang, F., Li, H., Li, Y. & Huang, X. (2011). [Response of glacier area variation to climate change in Chinese Tianshan mountains in the past 50 years.] *Acta Geogr. Sinica*, **66**(1), January, 38–46.

Wang, X., Ding, Y., Liu, S., Jiang, L., Wu, K., Jiang, Z. & Guo, W. (2013). Changes of glacial lakes and implications in Tian Shan, central Asia, based on remote sensing data from 1990 to 2010. *Environ. Res. Lett.*, **8**(4), October–December, 575–591. (doi: 10.1088/1748-9326/8/4/044052.)

Wei, J., Liu, S., Guo, W., Yao, X., Xu, J., Bao, W. & Jiang, Z. (2014). Surface-area changes of glaciers in the Tibetan Plateau interior area since the 1970s using recent Landsat images and historical maps. *Ann. Glaciol.*, **55**(66), 213–222. (doi: 10.3189/2014AoG66A038.)

Wei, J., Liu, S., Xu, J., Guo, W., Bao, W., Shangguan, D. & Jiang, Z. (2015). Mass loss from glaciers in the Chinese Altai Mountains between 1959 and 2008 revealed based on historical maps, SRTM, and ASTER images. *J. Mtn Sci.*, **12**(2), March, 330–343. (doi: 10.1007/s11629-014-3175-1.)

~~Werner, C., Wegmüller, U., Strozzi, T. & Wiesmann, A. (2001). Gamma SAR and interferometric processing software. *In* Sawaya-Lacoste, H., *ed. Proceedings of the ERS-Envisat Symposium: Looking down to Earth in the new millennium, Gothenburg, Sweden, 16–20 October 2000*, Noordwijk, European Space Agency, 9 pp., digital media. (https://www.gamma-rs.ch/uploads/media/2000-1_GAMMA_Software.pdf.)~~

Wu, K., Liu, S., Guo, W., Wei, J., Xu, J., Bao, W. & Yao, X. (2016). Glacier change in the western Nyainqentanglha Range, Tibetan Plateau using historical maps and Landsat imagery: 1970–2014. *J. Mtn Sci.*, **13**(8), August, 1358–1374. (doi: 10.1007/s11629-016-3997-0.)

Wu, K., Liu, S., Jiang, Z., Xu, J., Wei, J. & Guo, W. (2018). Recent glacier mass balance and area changes in the Kangri Karpo Mountains from DEMs and glacier inventories. *Cryosphere (TC)*, **12**(1), January, 103–121. (doi: 10.5194/tc-12-103-2018.)

Xu, J., Liu, S., Zhang, S., Guo, W. & Wang, J. (2013). Recent changes in glacial area and volume on Tuanjiefeng Peak region of Qilian Mountains, China. *PLOS ONE*, **8**(8), 27 August, e70574. (doi: 10.1371/journal.pone.0070574.)

Yang, K., Wu, H., Qin, J., Lin, C., Tang, W. & Chen, Y. (2014). Recent climate changes over the Tibetan Plateau and their impacts on energy and water cycle: a review. *Global Planet. Change*, **112**, January, 79–91. (doi: 10.1016/j.gloplacha.2013.12.001.)

Yang, W., Yao, T., Xu, B., Wu, G., Ma, L. & Xin, X. (2008). Quick ice mass loss and abrupt retreat of the maritime glaciers in the Kangri Karpo Mountains, southeast Tibetan Plateau. *Chin. Sci. Bull.*, **53**(16), August, 2547–2551. (doi: 10.1007/s11434-008-0288-3.)

Yang, W., Yao, T., Xu, B., Ma, L., Wang, Z. & Wan, M. (2010). Characteristics of recent temperate glacier fluctuations

in the Parlung Zangbo River basin, southeast Tibetan Plateau. *Chin. Sci. Bull.*, **55**(20), July, 2097–2102. (doi: 10.1007/s11434-010-3214-4.)

Yang, W., Yao, T., Guo, X., Zhu, M., Li, S. & Kattel, D.B. (2013). Mass balance of a maritime glacier on the southeast Tibetan Plateau and its climatic sensitivity. *J. Geophys. Res. Atmos.*, **118**(17), 16 September, 9579–9594. (doi: 10.1002/jgrd.50760.)

Yao, T., Ren, J. & Xu, B. (2008). *[Map of glaciers and lakes on the Tibetan Plateau and adjoining regions.]* (Scale: 1:2,000,000.) Xi'an, Xi'an Cartographic Publishing House. Lanzhou Institute of Glaciology and Geocryology. (In Chinese)

Yao, X., Liu, S., Guo, W., Huai, B., Sun, M. & Xu, J. (2012). [Glacier change of Altay Mountain in China from 1960 to 2009 – based on the Second Glacier Inventory of China.] *[J. Natur. Resour.]*, **27**(10), 1734–1745. (In Chinese with English summary.)

Yao, X., Liu, S., Zhu, Y., Gong, P., An, L. & Li, X. (2015). [Design and implementation of an automatic method for deriving glacier centerlines based on GIS.] *[J. Glaciol. Geocryol.]*, **37**(6), 1563–1570. (In Chinese with English summary)

Yao, T., Thompson, L., Yang, W., Yu, W., Gao, Y., Guo, X., Yang, X., Duan, K., Zhao, H., Xu, B., Pu, J., Lu, A., Xiang, Y., Kattel, D.B. & Joswiak, D. (2012). Different glacier status with atmospheric circulations in Tibetan Plateau and surroundings. *Nature Clim. Change*, **2**(9), September, 663–667. (doi: 10.1038/nclimate1580.)

Ye, Q., Zhong, Z., Kang, S., Stein, Alfred, Wei, Q. & Liu, J. (2009). Monitoring glacier and supra-glacier lakes from space in Mt. Qomolangma region of the Himalayas on the Tibetan Plateau in China. *J. Mtn Sci.*, **6**(3), September, 211–220. (doi: 10.1007/s11629-009-1016-4.)

You, Q., Kang, S., Pepin, N., Flügel, W.-A., Yan, Y., Behrawan, H. & Huang, J. (2010). Relationship between temperature trend magnitude, elevation and mean temperature in the Tibetan Plateau from homogenized surface stations and reanalysis data. *Global Planet. Change*, **71**(1–2), March, 124–133. (doi: 10.1016/j.gloplacha.2010.01.020.)

Zhang, Z., Liu, S., Wei, J., Xu, J., Guo, W., Bao, W. & Jiang, Z. (2016a). Mass change of glaciers in Muztag Ata–Kongur Tagh, eastern Pamir, China from 1971/76 to 2013/14 as derived from remote sensing data. *PLOS ONE*, **11**(1), 20 January, e0147327. (doi: 10.1371/journal.pone.0147327.)

Zhao Y, Zhu J. Assessing Quality of Grid Daily Precipitation Datasets in China in Recent 50 Years[J]. Plateau Meteorology, 2015, 34(1):50-58. (doi:10.7522/j.issn.1000-0534.2013.0014.) (In Chinese with English summary)

Zhang, Z., Xu, J., Liu, S., Guo, W., Wei, J. & Feng, T. (2016b). Glacier changes since the early 1960s, eastern Pamir, China. *J. Mtn Sci.*, **13**(2), February, 276–291. (doi: 10.1007/s11629-014-3172-4.)

Zhou, Y., Li, Z., Li, J., Zhao, R. & Ding, X. (2018). Glacier mass balance in the Qinghai–Tibet Plateau and its surroundings from the mid-1970s to 2000 based on Hexagon KH-9 and SRTM DEMs. *Rem. Sens. Environ.*, **210**, 1 June, 96–112. (doi: 10.1016/j.rse.2018.03.020.)

Zwally, H.J., Li, J., Brenner, A.C., Beckley, M., Cornejo, H.G., DiMarzio, J., Giovinetto, M.B., Neumann, T.A., Robbins, J., Saba, J.L., Yi, D. & Wang, W. (2011). Greenland ice sheet mass balance: distribution of increased mass loss with climate warming; 2003–07 versus 1992–2002. *J. Glaciol.*, **57**(201), 88–102. (doi: 10.3189/002214311795306682.)